이학석사 학위논문

Energy Calibration and MC Study of Cosmic Ray Induced Li & He Background at RENO

RENO 에너지 보정과
리튬, 헬륨 백그라운드에 대한 몬테카를로 연구

2014년 8월

서울대학교 대학원
물리천문학부
이 순 규

Abstract

RENO experiment is a reactor experiment for neutrino oscillation parameter θ_{13}. For successful measurement of θ_{13}, several things are needed. One of them is a regular detector calibration to maintain detector response during experiment period. By the energy calibration of detector, we get the constant detector response within $\sim 1.3\%$ error from begin of experiment, 2011.08. to 2014.04.

Another for successful experiment is to reduce background in detecting anti-neutrino. Beta-neutron decay of cosmogenic isotopes ^{9}Li and ^{8}He is the largest background in RENO. We have studied the ^{9}Li and ^{8}He background based on a Monte Carlo simulation and obtain estimated the ratio of ^{9}Li and ^{8}He production in detector. The ratio is 98.3%, $1.74 \pm 5.08\%$ for far detector, 88.3%, $11.7 \pm 4.40\%$ for near detector, Li and He respectively.

Keywords : **RENO, Neutrino oscillation, θ_{13}, Energy calibration, Monte Carlo simulation, ^{9}Li and ^{8}He background**

Student Number : 2011-23277

Contents

List of Figures

List of Tables

Chapter 1

Overview

1.1 Introduction

After the discovery of the neutrino oscillation that indicates physics beyond Standard Model, there has been neutrino experiments to measure parameters associated with neutrino mass and mixing and figure out their relations.

Among the several types of neutrino experiments, reactor neutrino experiment is to measure θ_{13}, one of neutrino oscillation mixing angles, by comparing measured neutrino fluxes at different distance from reactors. To reduce systematic errors such as ambiguities of neutrino flux, two or more detectors should be identical.

Although reactor experiment does not obtain any quantities of CP violation, θ_{13} is the crucial parameter to measure them. So θ_{13} is the key to other neutrino experiments, such as neutrino accelerators or experiments for CP violation. CP violation is fulfilled only if $\sin^2 2\theta_{13}$

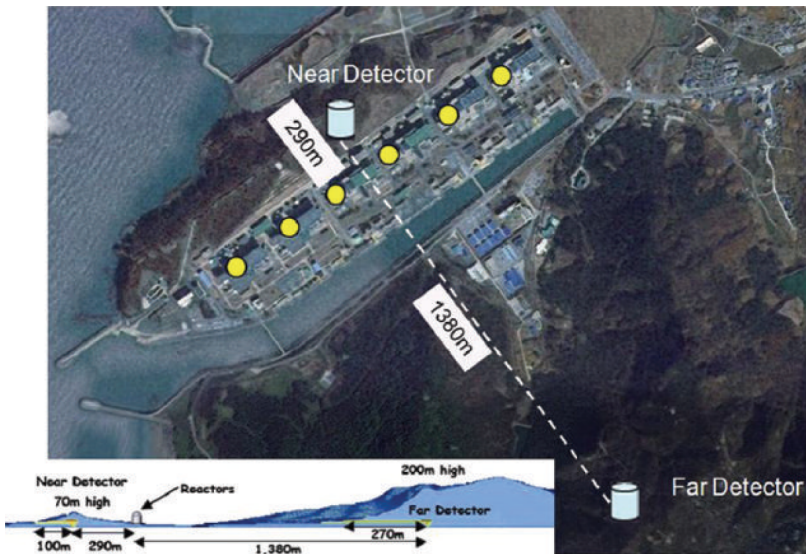

Figure 1.1: A schematic setup of RENO Experiment. This figure is taken from [2]

is greater than or equal to on the order of 0.01 [1].

1.2 The RENO experiment

The RENO is reactor experiments for neutrino oscillation to measure the precise value of θ_{13} based on the disappearance of antineutrinos. The RENO is located in Hanbit nuclear power plant, South Korea. The nuclear power plant has six reactors producing 16.4GW total power output.

1.2.1 Two Identical Detectors

In RENO, there is two identical detectors to reduce systematic uncertainties. One is located 290m from center of six reactors and is called

near detector. One located 1380m from center of reactors and is called far detector. Near detector is under 70m ridge that provides a depth of $\sim$110m water equivalent underground. Far detector is under 260m mountain, a depth of $\sim$450m water equivalent underground to reduce the cosmic ray background. [3] Schematic setup of RENO experiment is shown in Figure 1.1.

Although near may have more cosmic rays background than far because of location depth, the ratio of neutrino signals and backgrounds in near detector is higher than far due to shorter distance from reactors.

RENO detector consists of a neutrino target, a γ-catcher, a buffer, and a veto. Schematic view of RENO detector is shown in Figure 1.2. They are divided as a inner detector(ID) and a outer detector(OD). Inner detector has 354 photomultiplier tubes(PMTs) mounted on its inner wall and contains a target, a γ-catcher, and a buffer. Outer detector has 67 PMTs mounted on its inner wall and contains a veto and ID. The detector size is summarized in Table 1.1.

The target is the innermost layer and filled with 0.1 % Gd loaded liquid(Gd-LS) scintillator. Hydrogen, free proton, in Gd-LS is the target of neutrino for inverse beta decay(IBD) process. And Gd and H in Gd-LS can capture produced IBD neutrons and emit several γs.

The γ-catcher reduces γs that escape from target without depositing energy and it is filled with Gd-free liquid scintillator unlike the target region. The target and the γ-catcher are surrounded by transparent acrylic vessel that transmits up to 92 % for visible light [3].

The buffer is surrounded by stainless steal vessel to exclude light

Detector Component	O.D. (mm)	O.H. (mm)	Thickness(mm)	Material	V (m^3)	M (tons)
Target	2750	3150	-	Gd-LS	18.70	16.08
Target Vessel	2800	3200	25	Acrylic	0.99	1.18
γ-catcher	3940	4340	570	LS	33.19	28.55
γ-catcher Vessel	4000	4400	30	Acrylic	2.38	2.38
Buffer	5388	5788	694	Oil	76.46	64.22
Buffer Vessel	5400	5800	6 or 8*	SUS	1.05	8.39
Veto	8388	8788	1494	Water	352.61	352.61

Table 1.1: Dimensions of structure of RENO detector. Where O.D. is outer diameter and O.H. is outer height. (*)The buffer vessel thickness is 6 mm for the top and barrel sections and 12 mm for the bottom sections [3]. And this table is taken from [3] with some correction.

from outside of ID and filled with non-scintillating liquid(mineral oil). 354 PMTs are mounted on inner surface of buffer vessel to collect light from ID signal. The PMTs in the buffer provide 14 % photo-sensitive surface area coverage [3].

The veto reduces amount of backgrounds in ID such as cosmic rays and cosmic ray induced backgrounds. It is the outermost layer filled with purified water and is surrounded by 40cm thick concrete. 67 PMTs are mounted on inner surface of veto vessel to collect light of Cerenkov photons in water.

All PMTs in RENO detector are 10-inch photomultipliers and are shielded by mu-metal to reduce the noise from earth's magnetic field.

1.3 Neutrino Oscillation

According to current standard three neutrino theory, there are three neutrino flavor mixing angles, θ_{12}, θ_{23}, θ_{13}. One of them, θ_{12} is

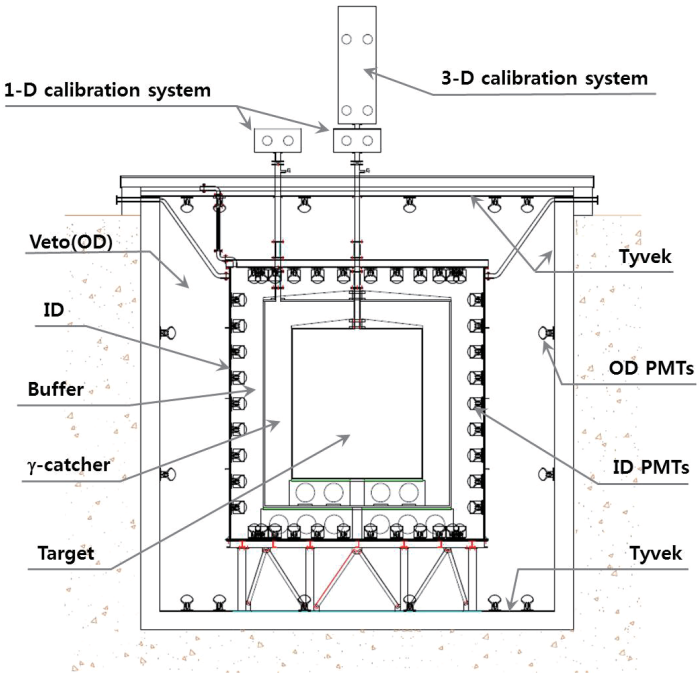

Figure 1.2: A schematic view of RENO detector. This figure is taken from [4]

found by solar neutrino at KamLAND. Another one, θ_{23} is found by atmosphere neutrino at K2K. [3]

1.3.1 Neutrino Mixing

Neutrino mass eigenstate $|\nu_i\rangle$ has definite energy eigenvalue, E_i corresponding to mass m_i. Because it is assumed that all massive neutrino have the same momentum $\vec{p}$ and mass of neutrino is very small compared with their momentum, energy eigenvalue can be approximated as

$$E_i = \sqrt{p^2 + m_i^2} \approx E + \frac{m_i^2}{2E} \tag{1.1}$$

Neutrino flavor eigenstates are related to mass eigenstates by a simple unitary transformation,

$$
\begin{aligned}
|\nu_\alpha\rangle &= U_{\alpha i}|\nu_i\rangle \\
|\nu_i\rangle &= U^*_{\alpha i}|\nu_\alpha\rangle
\end{aligned}
\tag{1.2}
$$

where α is neutrino flavor index ($\alpha = e, \mu, \tau$), i is neutrino mass index (i = 1, 2, 3). Time evolution of flavor eigenstate is

$$
|\nu_\alpha; t\rangle = U_{\alpha i} e^{-iE_i t}|\nu_i\rangle = U_{\alpha i} e^{-i(E+m_i^2/2E)t}|\nu_i\rangle \tag{1.3}
$$

PMNS(Pontecorvo-Maki-Nakagawa-Sakata) matrix $U_{\alpha i}$ can describe the neutrino mixing between flavor and mass eigenstates. According to standard theory of three neutrino flavors, matrix is given as follows [5–7],

$$
\begin{aligned}
U &= \begin{pmatrix} U_{e1} & U_{e2} & U_{e3} \\ U_{\mu 1} & U_{\mu 2} & U_{\mu 3} \\ U_{\tau 1} & U_{\tau 2} & U_{\tau 3} \end{pmatrix} \\
&= \begin{pmatrix} 1 & 0 & 0 \\ 0 & c_{23} & s_{23} \\ 0 & -s_{23} & c_{23} \end{pmatrix} \begin{pmatrix} c_{13} & 0 & s_{13}e^{-i\delta} \\ 0 & 1 & 0 \\ -s_{13}e^{i\delta} & 0 & c_{13} \end{pmatrix} \begin{pmatrix} c_{12} & s_{12} & 0 \\ -s_{12} & c_{12} & 0 \\ 0 & 0 & 1 \end{pmatrix}
\end{aligned}
\tag{1.4}
$$

$$
= \begin{pmatrix} c_{12}c_{13} & s_{12}c_{13} & s_{13}e^{-i\delta} \\ -s_{12}c_{23} - c_{12}s_{23}s_{13}e^{i\delta} & c_{12}c_{23} - s_{12}s_{23}s_{13}e^{i\delta} & s_{23}c_{13} \\ s_{12}s_{23} - c_{12}c_{23}s_{13}e^{i\delta} & -c_{12}s_{23} - s_{12}c_{23}s_{13}e^{i\delta} & c_{23}c_{13} \end{pmatrix}
$$

where $c_{ij} = \cos\theta_{ij}$, $s_{ij} = \sin\theta_{ij}$, and δ is the Dirac CP violating phase. If the mixing angles are all zero, then $U_{\alpha i}$ is identity matrix and there is no neutrino oscillation and flavor and mass eigenstate would be same respectively each generations. However the mixing angles are non-zero and the PMNS matrix with current oscillation parameter values is given [3],

$$U \approx \begin{pmatrix} 0.8 & 0.5 & < 0.2 \\ 0.4 & 0.6 & 0.7 \\ 0.4 & 0.4 & 0.7 \end{pmatrix} \tag{1.5}$$

Probability that ν_α with energy E changes to ν_β after time t, $P(\nu_\alpha \to \nu_\beta)$ is as follows

$$\begin{aligned} P(\nu_\alpha \to \nu_\beta) &= |\langle \nu_\alpha | \nu_\beta; t \rangle|^2 \approx |\langle \nu_\alpha | \nu_\beta; L \rangle|^2 \\ &= \left| \langle \nu_i | \, U^*_{\alpha i} U_{\beta j} e^{-iE_j t} \, | \nu_j \rangle \right|^2 = U^*_{\alpha i} U_{\beta i} U_{\alpha j} U^*_{\beta j} \exp\left(-i \frac{\Delta m^2_{ij} L}{2E} \right) \\ &= \delta_{\alpha\beta} - 4 \sum_{j<k} Re(U_{\alpha j} U^*_{\beta j} U^*_{\alpha k} U_{\beta k}) \times \sin^2\left(\frac{\Delta m^2_{jk} L}{4E} \right) \\ &- 2 \sum_{j<k} Im(U_{\alpha j} U^*_{\beta j} U^*_{\alpha k} U_{\beta k}) \times \sin^2\left(\frac{\Delta m^2_{jk} L}{2E} \right) \end{aligned} \tag{1.6}$$

neutrino travels distance L in vacuum during time t with nearly light velocity ($t \approx L$), where $\Delta m^2_{ij} \equiv m^2_i - m^2_j$

Isotope	Energy (MeV)
^{235}U	201.7±0.6
^{238}U	205.0±0.9
^{239}Pu	210.0±0.9
^{241}Pu	212.4±1.0

Table 1.2: Energy release per fission from [3]

1.3.2 Neutrino Flux from Reactors

If the main nuclear fuels of Hanbit reactors are four isotopes, ^{235}U, ^{238}U, ^{239}Pu and ^{241}Pu, average total number of $\bar{\nu}_e$ per fission is 6 and average energy release is 205MeV per fission as in Table 1.2. So the number of anti-neutrinos produced from total average 16.4 GW in Hanbit reactors,

$$\begin{aligned} N_\nu &= (\text{number of } \nu \text{ per fisson}) \times (\text{energy from reactors})/(\text{energy per fisson}) \\ &= (6) \times (1.64 \times 10^{10} J/s)/(3.28 \times 10^{-11} J) \\ &= 3 \times 10^{21} s^{-1} \end{aligned} \tag{1.7}$$

where (energy per fission), $205 MeV = 2.05 \times 10^8 eV \times 1.602 \times 10^{-19} J/eV = 3.28 \times 10^{-11} J$.

3×10^{21} $\bar{\nu}_e$ are produced per second in Hanbit reactors.

1.4 Inverse Beta Decay

The electron antineutrinos from reactor are detected via inverse beta decay, IBD, process. The process is as follows:

$$p + \bar{\nu_e} \rightarrow n + e^+$$

When an electron antineutrino produces a neutron and a positron, the resulting positron immediately annihilates and emits two gammas with visible energy, $1.022\text{MeV} + \text{K.E.}(\bar{\nu_e})$, that is called prompt signal. And the produced neutron is thermalized and then captured by Gd emitting several gammas with total visible energy $\sim$ 8MeV or captured by H emitting a gamma with $\sim$ 2.2MeV. These neutron capture processes take average time $\sim$ 28μs, so that is called delayed signal.

The energy threshold of IBD is $\sim$ 1.8 MeV, the sum of positron's mass(0.511 MeV) and mass difference between proton and neutron(1.293 MeV). Neutrino energy, $E_{\bar{\nu_e}}$ can be reconstructed by the energy of prompt energy, E_{prompt} as

$$\begin{aligned} E_{\bar{\nu_e}} &\approx K.E(\bar{\nu_e}) + 1.8\text{MeV} \\ &\approx E_{prompt} + 0.8\text{MeV} \end{aligned}$$

The energy of prompt signal is order of $10^0 \sim 10^1$ MeV, so the energy of antineutrino is same order. In RENO detector, there is no possibility that μ or τ antineutrino is detected.

1.4.1 Experiments Results

RENO begin data taking from August, 2011 and the best fit value of $\sin^2(2\theta_{13})$ is 0.101 $\pm$ 0.008 (stat) $\pm$ 0.010 (syst.) based on a rate only analysis during $\sim$800 days.

Chapter 2

Energy Calibration of RENO

2.1 Introduction

For the successful measurement of θ_{13} , it is important to calibrate two detectors' performance during long-term experiment period. Specifically, to pairing prompt and delayed signals, energy response of two detectors should be calibrated very well corresponding to IBD signals' energy range, $1 \sim 10$MeV. Also electronics may change its performance and LS in detector may change its properties such as attenuation length and scintillation, so calibration should be regularly carried out to monitor detector.

The goal of energy calibration is to obtain conversion function between the number of photo-electrons from PMTs and the energy of particles. Another goal is to maintain constant detector response

during experiment period with reasonable correction.

2.2 DAQ Process

2.2.1 Front-End Electronics

When an optical photon reaches a PMT, a PMT gives signals in accordance with probability. QBEE, QTC(charge-to-time converter) based on electronics with an onboard ethernet card, is used as ADC electronics in RENO. Each QBEE board has an 100Mbs ethernet card. A QBEE board has 4 TDC chips and 8 QTC chips. Each QTC chip has 3 input channel, so total 24 channels per a QBEE board. In RENO 18 QBEE boards that have total 1.8Gbs is used for 421 PMTs at each detectors.

The QTC chip receives PMT pulses and measure hit time, and charge of the pulse and then convert them. The leading edge of pulse is regarded as hit arrival time. When a pulse exceeds a current threshold, the capacitor in QTC integrates charge, it called charging gate and discharge with constant amount so a period discharging time is proportional to the size of integrated charge. During the discharging period, any next signals are ignored. The processing time of QTC is $\sim 1\mu s$ per cycle. The characteristics of QTC chips is summarized in Table 2.1.

4 TDC in QTC receive external clock of 60MHz and a periodical trigger signal of 60KHz from a master clock. 60KHz initializes TDC timing tag and event number that identifies PMT hits in same trigger.

Dynamic range	0∼2500pC
Self trigger	Built-in discriminator
Number of input channels	3
Processing speed	∼500ns/cycle
Gain	1/7/49 (3 settings)
Charge resolution	0.05p.e. (<25 p.e.)
(Non-) Linearity(Q)	< 1%
Timing resolution	0.3ns (1p.e.=-3mV), 0.2ns(>5p.e.)
Power dissipation	< 200mW/channel

Table 2.1: The characteristics of QTC chips in QBEE board. This table is taken from [3]. This table is the summary of the contents in [10, 11] with correction because QBEE is customized in RENO.

2.2.2 DAQ

DAQ components and run conditions can be controlled through run controller. 60KHz has serialized 32-bit number. And the hits are sorted and merged according to trigger event number and timing information. All hits are divided into certain window and constructed into events if sum of hits in a window exceeds a certain threshold.

In RENO all hits from PMTs over a certain threshold are all recoded and then are cut by software trigger. There are several trigger types. One is to pick out neutrino-like events in Buffer region and Another is to pick out cosmic ray muon like events in Veto region.

2.3 Energy Calibration

2.3.1 Radioactive Sources

To obtain IBD signals(photo-electrons) to the energy of particles(MeV) conversion function, following radioactive sources are used in RENO,

Type	Source	Energy(KeV)	Calibration
e^+	^{68}Ge	511(2)	positron E threshold
γ	^{137}Cs	662	gamma
	^{60}Co	1173+1333	multiple gammas
n	^{252}Cf	neutron	neutron efficiency

Table 2.2: List of the calibration sources in RENO. This table is taken from [3]

^{68}Ge(e^+), ^{60}Co(γ), ^{137}Cs(γ) and ^{252}Cf(neutron). These sources are selected considering emitted particles same with or similar to those of IBD events and energy range within the IBD's.

^{68}Ge decays into ^{68}Ga and ^{68}Ga positive beta decays emitting e^+. Produced e^+ mostly annihilates with electron in the surface of Ge source. It can be used for the calibration of positron energy threshold. ^{137}Cs beta decays into ^{137}Ba-m and ^{137}Ba-m gamma decays into stable ground state of ^{137}Ba emitting only one gamma. ^{60}Co(γ) decays into ^{60}Ni and ^{60}Ni emits two gammas. The properties of these radioactive sources are summarized in Table 2.2.

2.3.2 Source Driving System

The source driving system consists of the pulley system and glove box enclosing it. There are two pulley systems in each detector sites, one for target and the other for gamma-catcher region. The pulley system is driven by stepping motor and has polyethylene wire , acrylic case and a weight.

To prevent LS contaminations from radioactive sources, sources are capsulated by acrylic case during calibration. When radioactive

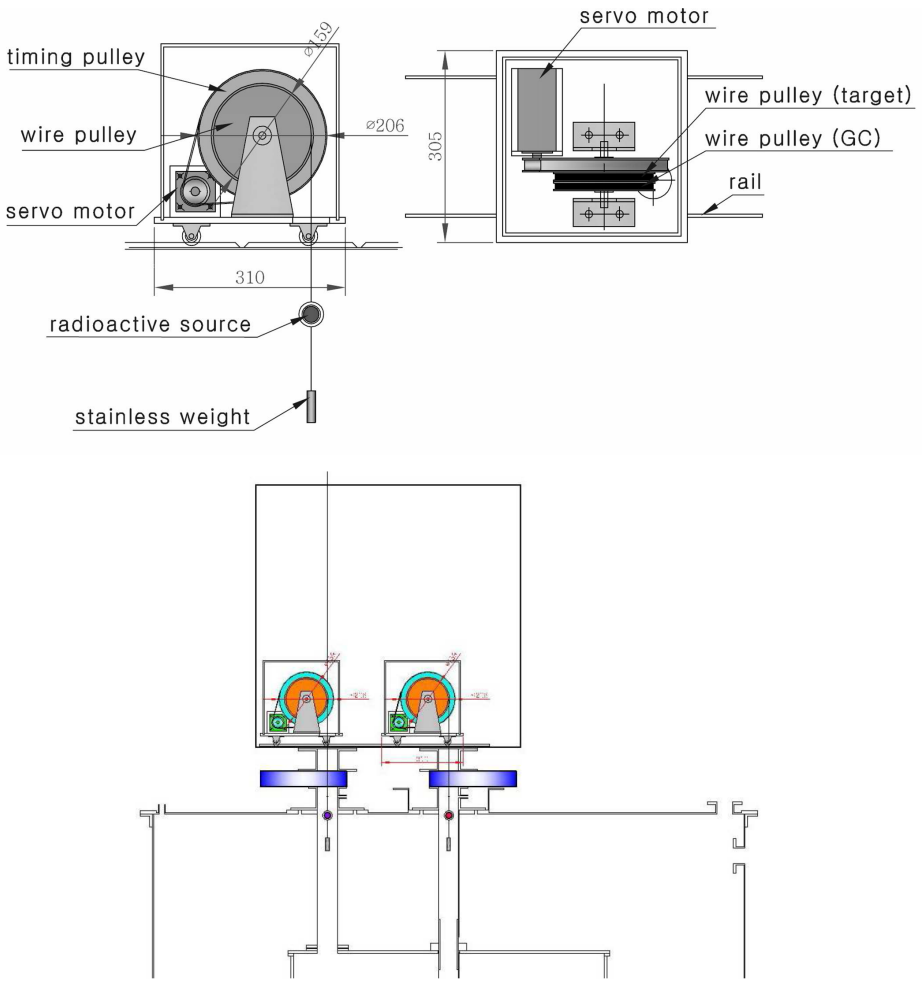

Figure 2.1: The source driving system for RENO detector. The weight connected at end of wire is not made of stainless but Teflon-PFA. These pictures are taken from [3]

Figure 2.2: An acrylic capsule of radioactive sources. There is ^{252}Cf source in acrylic capsule.

sources are in LS, a weight is attached at the case against buoyant force of LS. The connected weight is made of Teflon-PFA that is chemically stable with LS [3]. Acrylic case is shown in Figure 2.2.

The calibration source can move along z-axis in target or gamma-catcher region, which is used to understand the position dependence of signals' energy. The position resolution of the pulley system is $\sim$0.5mm.(It is average value over 20 times winding and unwinding wire of each pulley) [12]. The source driving system is shown in Figure 2.1.

2.3.3 Radioactive Source Response

When a gamma is created by radioactive sources in LS, it makes the atoms in LS excited and the number of excited atoms is proportional to the energy of the produced gamma if its total energy deposit to LS is sufficient. Then the excited states of the atoms emit visible light. Visible light strikes electrons at surface of PMTs and produces a photo-electron per one photon.

The energy response, n.p.e, from a gamma in RENO detector has broad distribution due to the energy transfer in LS above-mentioned and energy resolution of RENO detector.

The response difference between one gamma and multiple gammas can be compared by ^{137}Cs and ^{60}Co energy response. ^{68}Ge also produce two gammas. And there are two peaks in ^{256}Cf according to what neutron is captured by H or Gd.

In ^{137}Cs case, n.p.e distribution of single gamma is gaussian shape. This means that the energy of single gamma is sufficiently deposited in detector. And its peak value is similar to expectation value from calculation of light yield of LS, attenuation effects in LS, PMT coverage, PMT quantum efficiency, and the decay particle energy of source.

The peak value is regarded as the particle energy after applying follow several corrections. The difference between observed n.p.e and particle energy because of quenching effects of multiple gammas and the effects from acrylic case enclosing sources. These factors are applied to the data by MC simulation.

2.3.4 Energy Conversion Function

The energy of ^{137}Cs, 0.662MeV, is lower than the minimum energy of prompt signal 1.022MeV. And the neutron from ^{252}Cf can be captured by H or Gd. Fitting four points, excepting the point of ^{137}Cs, the p.e. to MeV conversion function is obtained. The difference between data points and fit function is within $\sim 0.1\,\%$. The result of energy calibration in RENO is shown in Figure 2.5. We plan to use more radioactive sources to get more precise conversion function.

2.3.5 Stability of Source Calibration

Detector performance is monitored by calibration source such as monitoring temporal change of radioactive sources response. In Figure 2.6 2.7 2.8, there are lines in each sub figures, they indicate a sudden change of peak value because of several reasons such as PMTs disconnection. If there are some problems in detector, these problems appear in temporal change of sources response regardless of source type. For example, in far detector we found UPS problem and removed UPS. Considering these problems, we correct detector response to produce constant value. After IBD pairing, we correct the energy of Gd delayed signal to be 8MeV, it is called charge correction. Charge corrected peak value is shown in lower part in sub figures. And the mean and error of charge corrected peak value is summarized in Table 2.3. Through charge correction, the detector response is stable within $\sim 1.3\%$ from the begin of data taking to 2014.04.16.

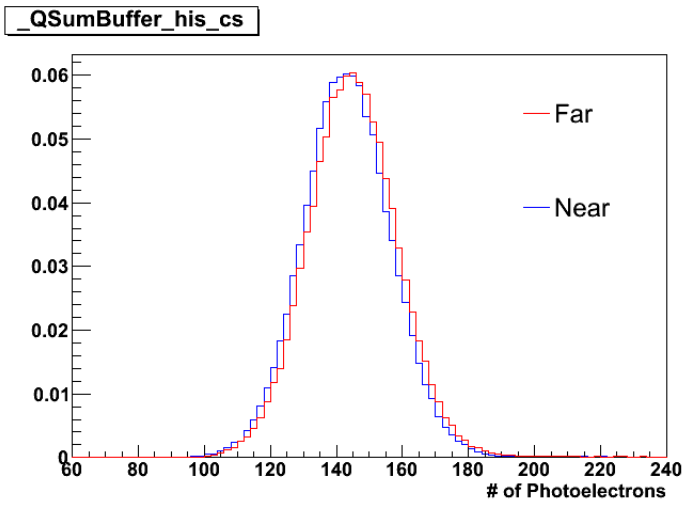

(a) ^{137}Cs Energy spectrum

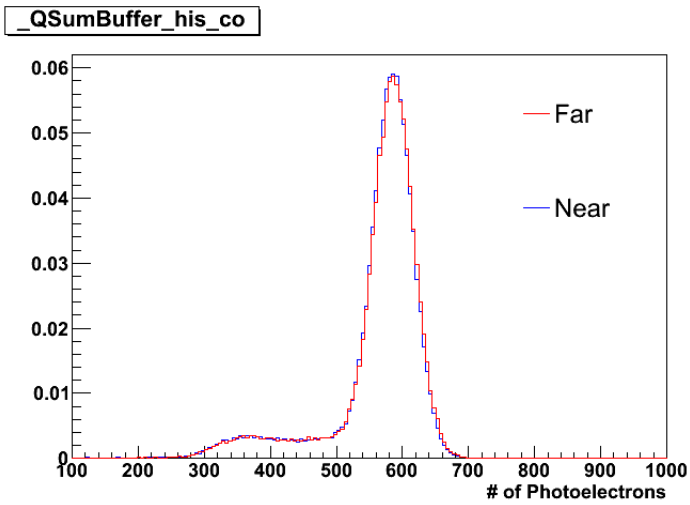

(b) ^{60}Co Energy spectrum

Figure 2.3: Energy spectrum of radioactive sources, ^{137}Cs, ^{60}Co

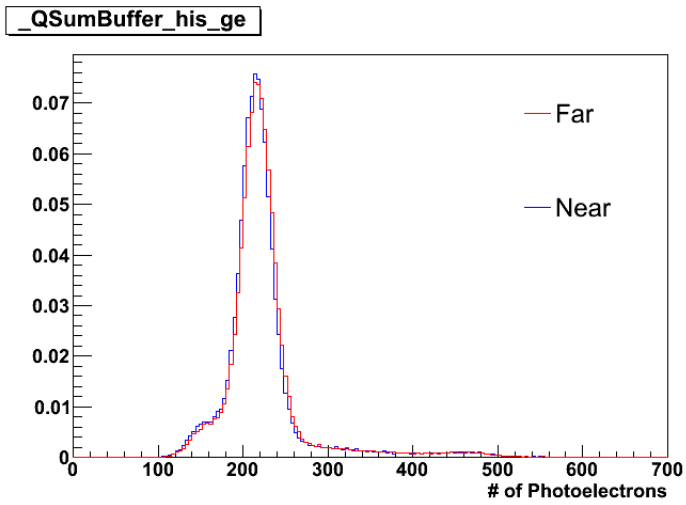

(a) ^{68} Ge Energy spectrum

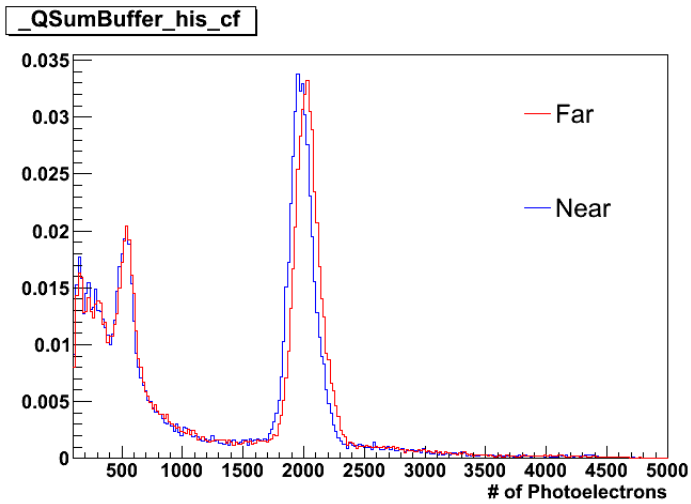

(b) ^{252} Cf Energy spectrum

Figure 2.4: Energy spectrum of radioactive sources, ^{68} Ge, ^{252} Cf

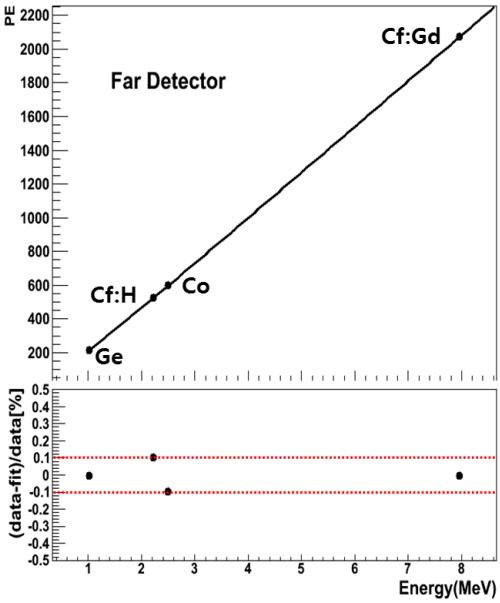

(a) Far Detector

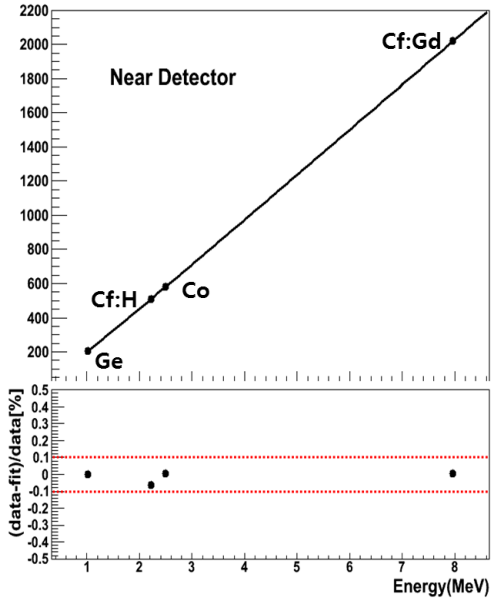

(b) Near Detector

Figure 2.5: Result of energy calibration in the far and near detector. This figure is taken from [13]

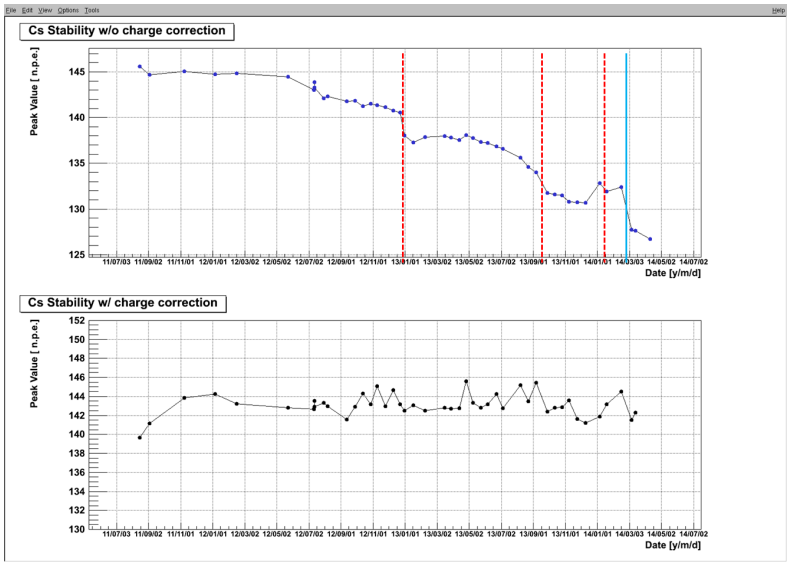

(a) Far ^{137}Cs

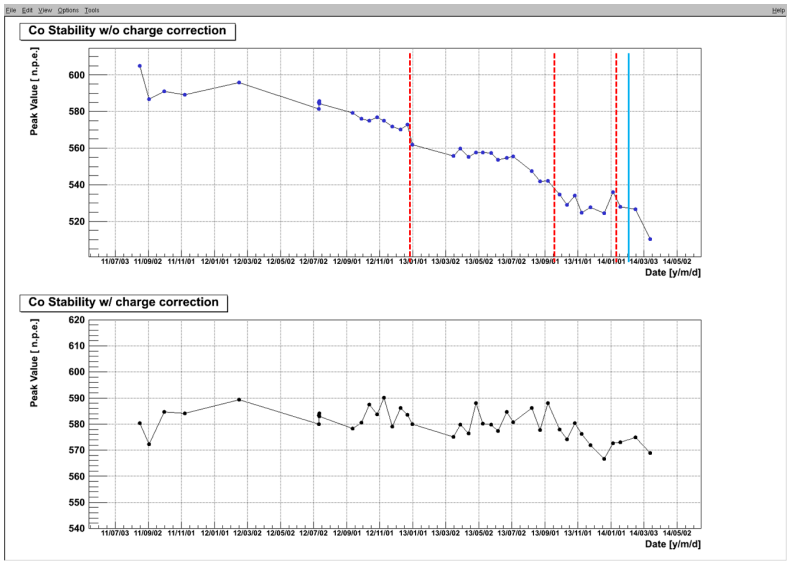

(b) Far ^{60}Co

Figure 2.6: Source calibration stability in far, near detector. Dashed line means the date of several PMTs disconnection. Full line (only in far) means the date of UPS removal. Peak value of n.p.e distribution with temporal change without correction in upper part and with correction in lower part in each sub figures.

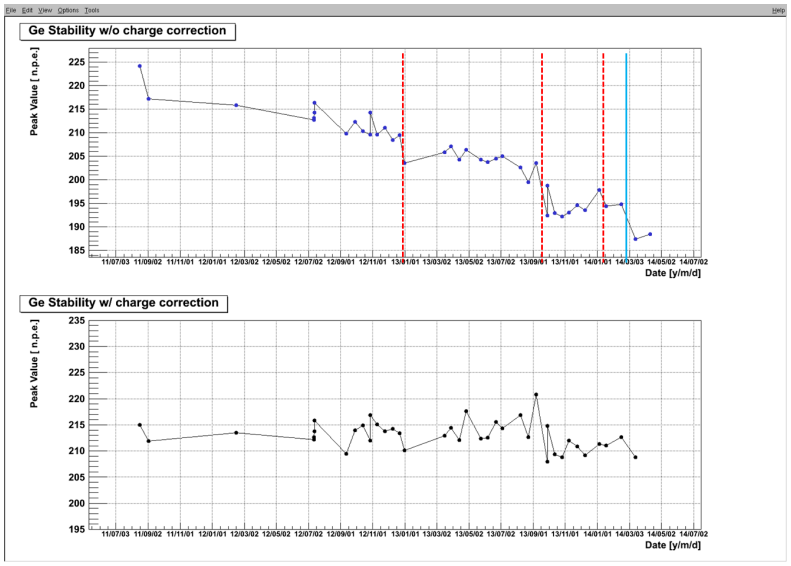

(a) Far ^{68}Ge

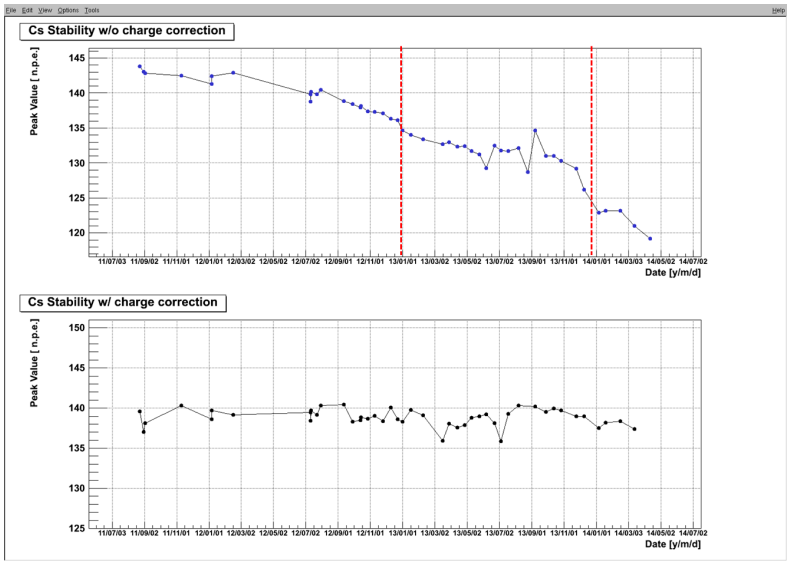

(b) Near ^{137}Cs

Figure 2.7: Source calibration stability in far, near detector. Dashed line means the date of several PMTs disconnection. Full line (only in far) means the date of UPS removal. Peak value of n.p.e distribution with temporal change without correction in upper part and with correction in lower part in each sub figures.

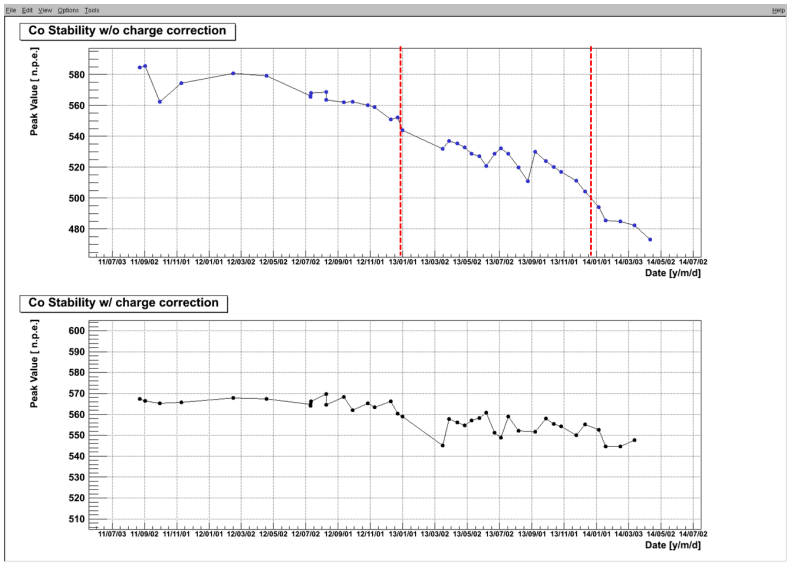

(a) Near ^{60}Co

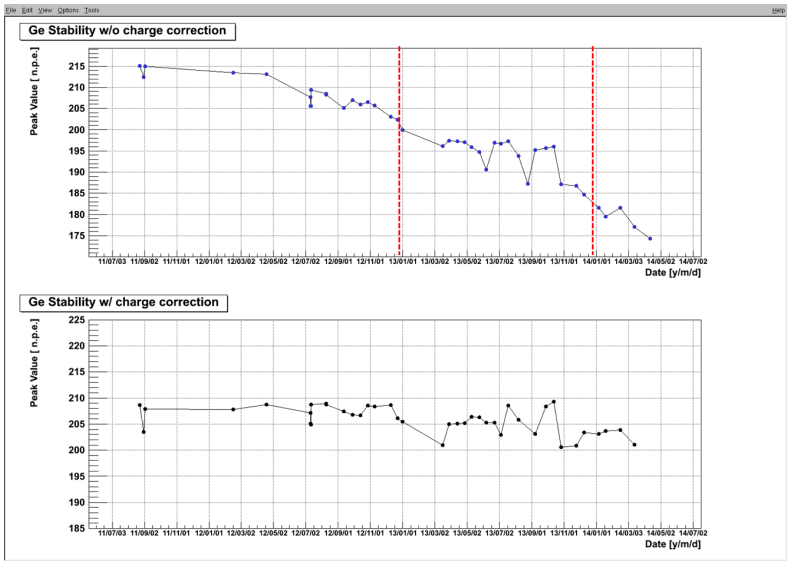

(b) Near ^{68}Ge

Figure 2.8: Source calibration stability in far, near detector. Dashed line means the date of several PMTs disconnection. Full line (only in far) means the date of UPS removal. Peak value of n.p.e distribution with temporal change without correction in upper part and with correction in lower part in each sub figures.

Source	Far	Near
^{137}Cs	143.2 ± 1.250	138.8 ± 1.043
	(0.873%)	(0.7514%)
^{68}Ge	213.0 ± 2.660	205.8 ± 2.503
	(1.249%)	(1.216%)
^{60}Co	580.0 ± 5.566	558.9 ± 7.219
	(0.9597%)	(1.2916%)

Table 2.3: The mean and error of charge corrected peak value. From 2011.08 to 2014.04 data. Through charge correction, detector responses are stable within $\sim$1.3%.

Chapter 3

MC Study of β-n Decays from ^{9}Li and ^{8}He

3.1 Introduction

Although systematic uncertainty in RENO is reduced greatly by using two identical detectors, beta decays from cosmogenic isotopes ^{9}Li and ^{8}He are irreducible systematic uncertainties and the largest backgrounds in the RENO experiment [13].

Ratio of background subtracted IBD rate and total background is 2.79% and 5.83%, far and near respectively. ^{9}Li and ^{8}He background rate occupies about 57% and 61% of total background rate, near and far respectively. The exact amount of IBD rate, total and Li/He background rate in RENO are in Table 3.1. And background means the signal mimicking IBD's.

^{9}Li and ^{8}He has several β-neutron emission decay modes which

gives signal mimicking prompt and delayed signal respectively. So this kind of background is indistinguishable from IBD signal unless additional conditions are used. Detailed explanations about ^{9}Li and ^{8}He 's characteristics are in Sect. 3.2.1.

^{9}Li and ^{8}He can be produced in detector when an atmospheric muon strikes ^{12}C in liquid scintillator passing through it and produces unstable isotopes. So we expect that ^{9}Li and ^{8}He productions are different in far, near site. And comparing the composite nucleons of ^{12}C with ^{9}Li and ^{8}He, ^{8}He requires higher moun energy to be produced than ^{9}Li. So we also expect that ^{9}Li has higher percentages of ^{9}Li and ^{8}He productions.

Simulation study of ^{9}Li and ^{8}He backgrounds can improve our understanding of these backgrounds.

Detector (per day)	Near	Far
IBD rate subtracted background	779.05 ± 6.26	72.78 ± 0.95
Total background rate	21.75 ± 5.93	4.24 ± 0.75
^{9}Li and ^{8}He background rate	12.45 ± 5.94	2.59 ± 0.75

Table 3.1: IBD and background rate(per day) of near and far detectors. This values are taken from [4]

3.2 ^{9}Li and ^{8}He β-n decay

3.2.1 ^{9}Li and ^{8}He β-decay characteristics

Unstable isotopes has mean lifetime 257ms for ^{9}Li and 172ms for ^{8}He. The Q values of ^{9}Li and ^{8}He β decay are 13.61 MeV and 10.65 MeV overlapping with positron signal of IBD. Some emitters

of ^{9}Li and ^{8}He have sufficient energy for neutron decay which can be captured by Gd. And this neutron decay occurs immediately because it competes with γ decay. Decay scheme of ^{9}Li and ^{8}He are in Figure 3.1.

The characteristics of ^{9}Li and ^{8}He are studied in [14–18]. Summary of these results is given in Table 3.2.

Parent	Daughter or Emitter	Γ(MeV)	BR	β	neutron
^{9}Li	^{9}Be (ground)	0	48.7	◯	×
^{9}Li	^{9}Be (2.43MeV)	0.00077	30	◯	◯
^{9}Li	^{9}Be (2.78MeV)	1.08	16	◯	◯
^{9}Li	^{9}Be (7.94MeV)	1.0	1.5	◯	◯
^{9}Li	^{9}Be (11.28MeV)	0.575	1.1	◯	◯
^{9}Li	^{9}Be (11.81MeV)	0.400	2.7	◯	◯
^{8}He	^{8}Li (0.98MeV)	0	84	◯	×
^{8}He	^{8}Li (3.21MeV)	1.0	12	◯	◯
^{8}He	^{8}Li (5.4MeV)	0.65	4	◯	◯

Table 3.2: The characteristics of ^{9}Li and ^{8}He, where Γ is the decay width and BR is brancing ratio. Both Decay width are from [14]. Branching ratio of ^{9}Li and ^{8}He are from [18], [14, 15] respectively.

3.2.2 Q value

In general, the beta decay of nucleus, ${}^{A}_{Z}X$, is expressed as follows.

$$ {}^{A}_{Z}X \rightarrow {}^{A}_{Z+1}X' + e + \bar{\nu_e} $$

We define Q value as the nuclear mass energy difference between reactants and products. It is the same definition with that of [19]. With

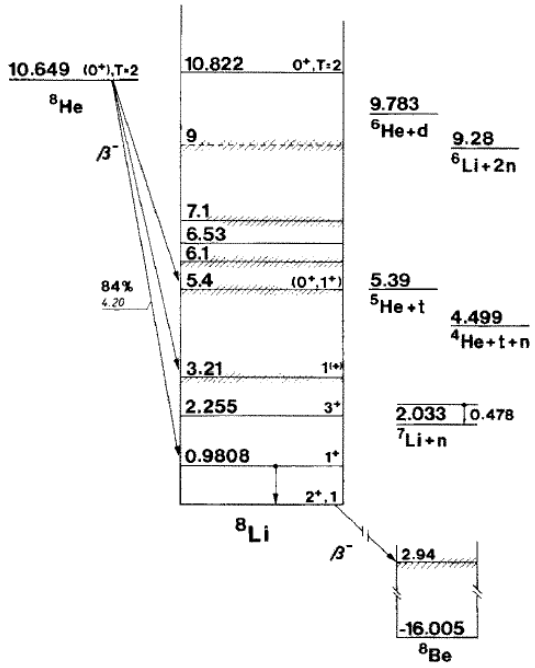

(a) ^{8}He decay scheme from [17]

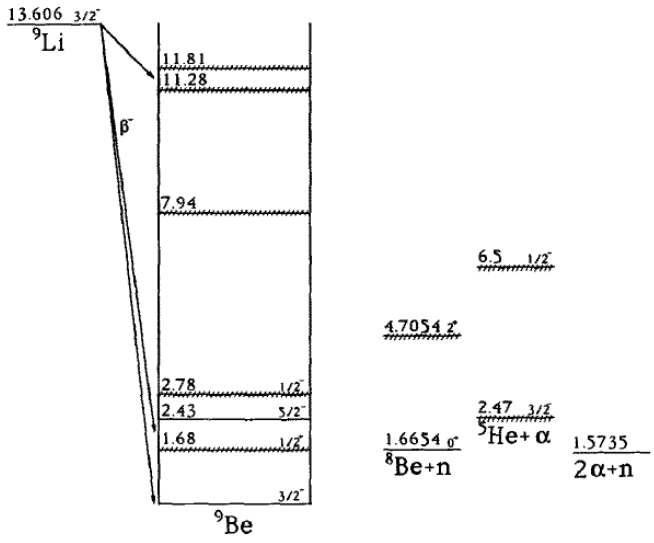

(b) ^{9}Li decay scheme from [15]

Figure 3.1: Decay scheme of ^{9}Li and ^{8}He

energy conservation Q value is given by in natural unit,

$$\begin{aligned} E_X &= E_{X'} + E_e + E_{\bar{\nu}_e} \\ T_X + m_x &= T_{X'} + m_{X'} + T_e + m_e + T_{\bar{\nu}_e} \\ T_X + Q &= T_{X'} + T_e + T_{\bar{\nu}_e} \\ Q &\approx T_e + T_{\bar{\nu}_e} \end{aligned}$$

because neutrino mass is nearly zero,

$$Q = T_e + p_\nu \tag{3.1}$$

where m_N is the nuclear masses, T is kinetic energy, p is momentum. So in nucleus beta decay kinetic energy of electron has maximum value Q and continuous spectrum of range [0 ,Q]. Of course in case of nucleus beta decay to excited daughter, Q value is modified, $Q' = Q - E^*$, where E^* is the excited energy level of daughter.

3.2.3 β decay spectrum

^{9}Li and ^{8}He has far longer lifetime than characteristic nuclear time, $\sim 10^{-20}$ s [19]. In fact, beta decay-causing interaction is weak interaction. Weak interaction is sufficient weak comparison with the interaction that forms quasi-stationary state, electromagnetic and strong interaction. So we take decay-causing interaction as weak perturbation. The transition rate is as follows, by Fermi Golden rule,

$$\lambda = \frac{2\pi}{\hbar} |V_{fi}|^2 \rho(E_f) \tag{3.2}$$

where V_{fi} is matrix element and $\rho(E_f)$ is density of states, $\rho(E_f) = dn/dE_f$ means the number dn of final states in the energy interval dE_f and $V_{fi} = \int \psi_f^* V \psi_i d\tau$. And Fermi express that operator V could be replaced with one of five mathematical operators O_x consistent with special relativity in his thesis [20, 21]. X = V(vector), A(axial vector), S(scalar), P(pseudoscalar), or T(tensor). And in final states, there are an electron, neutrino, and daughter nucleus. So,

$$V_{fi} = g \int [\psi_f^* \phi_e^* \phi_\nu^*] O_x \psi_i d\tau \tag{3.3}$$

where g is the constant that determines the strength of the interaction, ϕ_e^*, ϕ_ν^* is the eigenstate of electron and neutrino, respectively. $\rho(E_f)$ determines the shape of β energy spectrum. With momentum conservation of beta decay in CM frame, $\vec{p}_{X'} + \vec{p}_e + \vec{p}_\nu = 0$, the number dn is expressed by

$$dn = dn_e dn_\nu = \frac{(4\pi)^2 p_e^2 dp_e p_\nu^2 dp_\nu V^2}{h^6} \tag{3.4a}$$

$$dn_{e,\nu} = \frac{4\pi p_{e,\nu}^2 dp_{e,\nu} V}{h^3} \tag{3.4b}$$

Suppose ϕ_e^*, ϕ_ν^* has usual free-particle eigenstate, normalized with the volume V to see only shape of β spectrum.

$$\phi_{e,\nu}^* = \frac{1}{\sqrt{V}} \exp(i\vec{p}_{e,\nu} \cdot \vec{r}/\hbar) \tag{3.5}$$

If $T_e \approx 5\,\mathrm{MeV}$, $p_e = 10.5\,\mathrm{MeV}$, $p/\hbar = 0.05\ \mathrm{fm}^{-1}$, over nuclear volume, $p_e r/\hbar \ll 1$,

$$\exp(i\vec{p_{e,\nu}} \cdot \vec{r}/\hbar) = 1 + \frac{i\vec{p_{e,\nu}} \cdot \vec{r}}{\hbar} + \cdots \cong 1 \tag{3.6}$$

This approximation is called allowed approximation.

To obtain beta spectrum dependent only on p_e, partial decay rate for electrons is needed,

$$d\lambda(p_e) = \frac{2\pi}{\hbar} g^2 |M_{fi}|^2 (4\pi)^2 \frac{p_e^2 dp_e p_\nu^2}{h^6} \frac{dp_\nu}{dE_f} \tag{3.7}$$

where $M_{fi} \equiv \int \psi_f^* O_x \psi_i d\tau$ is nuclear matrix element

Final state energy ignoring small recoil energy of daughter nucleus is $dp_\nu/dE_f = dp_\nu/dE_\nu = 1$ with E_e fixed.

As far as the shape of the electron spectrum is concerned, the number of electrons with momentum between p_e and $p_e + dp_e$,

$$N(p_e)dp_e = C p_e^2 p_\nu^2 dp_e \tag{3.8}$$

In beta decay, electron also should be treated relativistically.

$$p_e^2 + m_e^2 = T_e^2 + 2m_e T_e + m_e^2$$
$$p_e = \sqrt{T_e^2 + 2m_e T_e}$$
$$dp_e = \frac{T_e + m_e}{\sqrt{T_e^2 + 2m_e T_e}} dT_e$$

With relativistic kinetic energy and energy conservation, Eq. (3.1),

$$N(T_e)dT_e = C\sqrt{T_e^2 + 2m_eT_e}(T_e + m_e)(Q - T_e)^2 dT_e \tag{3.9}$$

And correction for β's Coulomb interaction with a daughter nucleus, the Fermi function, should be applied. So,

$$N(T_e) \propto \sqrt{T_e^2 + 2m_eT_e}(T_e + m_e)(Q - T_e)^2 F(Z_d, T_e) \tag{3.10}$$

where $F(Z_d, T_e)$ is Fermi function, Z_d is the atomic number of daughter nucleus. This subsection 3.2.3 follows content development of [19].

3.3 MC simulation

3.3.1 Event generation for ^{9}Li and ^{8}He β-n decay

Event generation is a previous step for MC simulation. Event generation includes generating beta's position in detector and momentum of beta. Vertexes should be generated uniformly in detector sized place because beta decay can be occurred anywhere in detector. And also produced beta has the beta energy spectrum in Section 3.2.3. We use TRandom3 class of ROOT program to generate random variable.

For the generation of uniform vertexes inside a Buffer sized cylindrical region, (x, y, z) are uniformly generated in rectangular box and then set of (x, y) are rejected if it is out of $\rho = \sqrt{x^2 + y^2}$. The result is shown in Figure 3.2.

And for the momentum of beta, we already know beta momentum, p following the beta spectrum Eq. 3.10, we need Cartesian coordinate

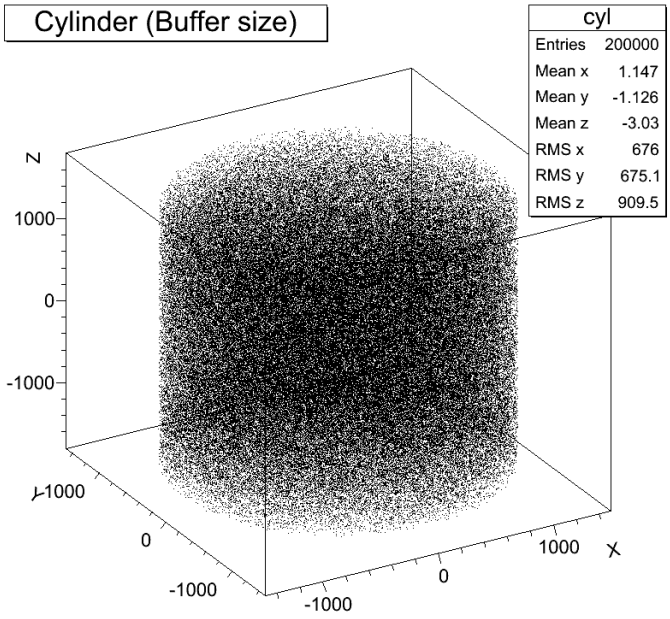

Figure 3.2: Random generation - Buffer size cylinder

component of momentum, p_x, p_y, p_z. So $p = \sqrt{p_x^2 + p_y^2 + p_z^2}$, momentum shell should be uniformly random generated. In spherical coordinate, $d\Omega = \sin\theta d\theta d\phi$, so we set $u = \cos\theta$ to satisfy $du = \sin\theta d\theta$, and then simply random generate u and ϕ uniformly. Then we obtain Cartesian components of momentum that distributed uniformly in spherical coordinate as follows.

$$p_x = p\sqrt{1-u^2}\cos\phi \tag{3.11}$$

$$p_y = p\sqrt{1-u^2}\sin\phi \tag{3.12}$$

$$p_z = pu \tag{3.13}$$

The result is shown in Figure 3.3.

Last, for beta energy spectrum, unstable QM state following the exponential decay has not definite but broad energy level. So the energy levels of decay-daughter are broad. The probability density of that energy eigenvalue is given as normalized Breit-Wigner formula. Breit-Wigner formula is driven in Appendix B.

Broad energy levels also give energy variations to the Q value of corresponding decay channel. And these energy variations follows the probability density, normalized Breit-Wigner formula. So it is applied as the variation of Q value in Eq. 3.10 with the probability of variation. Considering this process we generate sufficient events, order of 10^5. The decay widths of each decay channels are shown in Table 3.2, note that we consider only β-n decay channels.

After modification due to Breit-Wigner formula, beta spectrum is

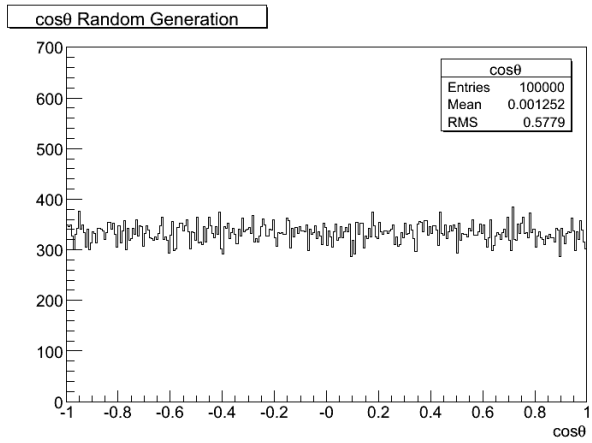

(a) $\cos\theta$ random generation

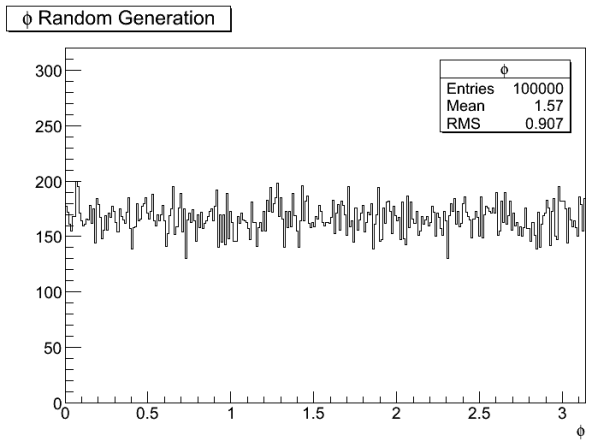

(b) ϕ random generation

Figure 3.3: Random generation - unit shell in momentum space

given.

$$N(T_e) \propto \int d(\Delta E) \frac{1}{(\Delta E)^2 + \frac{\Gamma^2}{4}} \sqrt{T_e^2 + 2m_e T_e}(T_e + m_e) \times (Q + \Delta E - T_e)^2 F(Z_d, T_e) \quad (3.14)$$

where ΔE is the energy variation due to Breit-Wigner formula and Γ is the decay width.

Fermi function, the correction factor for Coulomb interaction, $F(Z_d, T_e)$ is taken from Fermi function of Geant4 code. The result of event generations is shown in Figure 3.4, 3.5.

3.3.2 Detector simulation

Simulation tool is GLG4sim, Generic Liquid-scintillator Anti-neutrino Detector Geant4 simulation, that is derived from KGL4sim, a Geant4-based Monte Carlo for KamLAND.

Every event input particle is one electron that has energy of beta spectrum and is located anywhere in the buffer as mentioned in Section 3.3.1. Actual detector's characteristics are copied in simulation. But there are some deficiencies in simulation. One of them is that the effect caused by angle of incidence between optical photon and PMT, function of θ, is not applied in simulation. In other words, in simulation a PMT has the same response probability when optical photon touches the surface of it at any angle.

An input electron mainly interacts with the atoms of LS in detector and then finally the most energy of it is transferred to PMTs. So we get the detector energy response in simulation as n.p.e distribu-

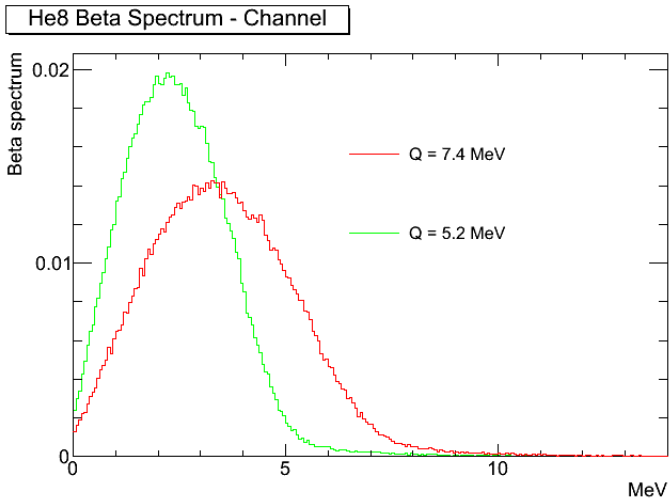

(a) ^{8}He β spectrum for each channel

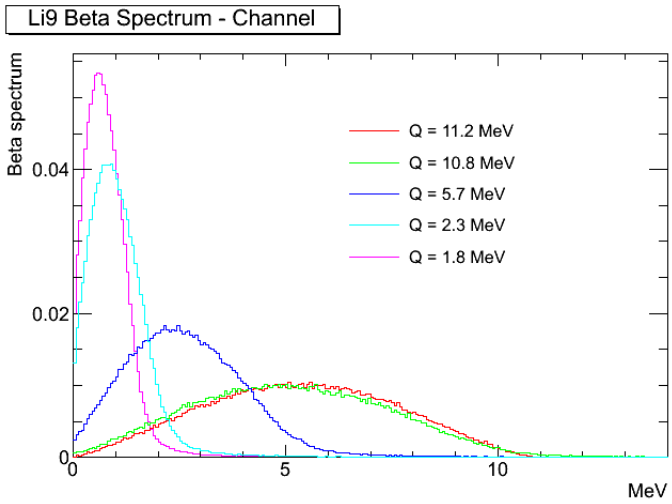

(b) ^{9}Li β spectrum for each channel

Figure 3.4: Random generation results. ^{8}He, ^{9}Li only β-n spectrum for each decay channel.

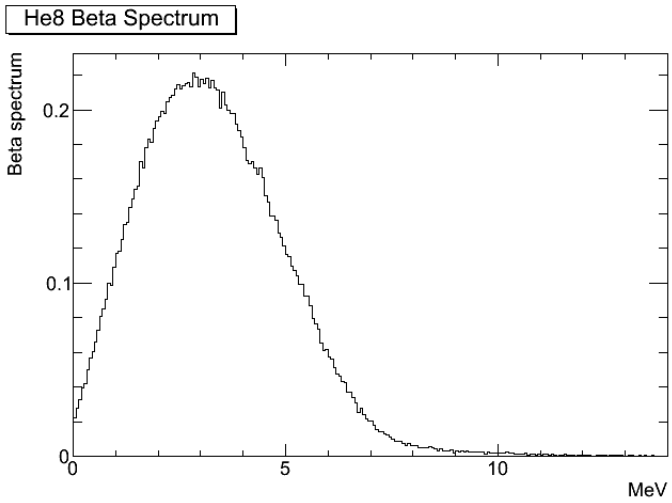

(a) ^{8}He β spectrum for all channels

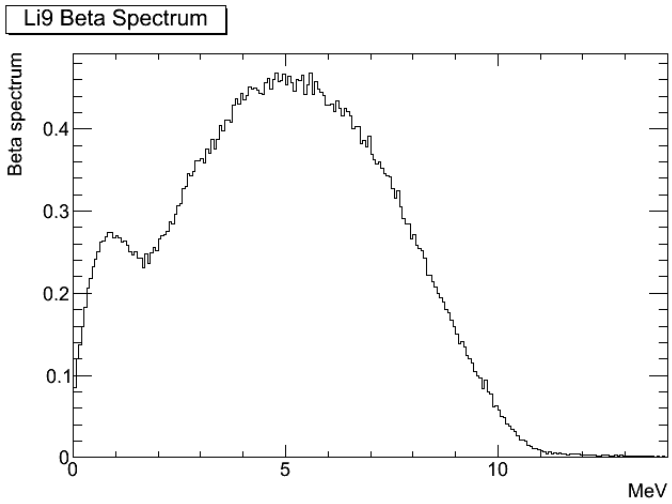

(b) ^{9}Li β spectrum for all channels

Figure 3.5: Random generation results. ^{8}He, ^{9}Li only β-n spectrum for total with branching ratio.

tion corresponding to the energy of input electron. Also the energy resolution of detector is applied. We use $2 \sim 5 \times 10^5$ events to obtain the beta spectrum of simulation.

The n.p.e. distribution results are shown in Figure 3.6, 3.7. In these figures, the beta spectrum of each decay channels or total channel is normalized, then y-axis of the histograms have arbitrary unit. But it doesn't matter because our goal of simulation is to fit the real ^{9}Li and ^{8}He background data with simulation results and to compare the shapes only.

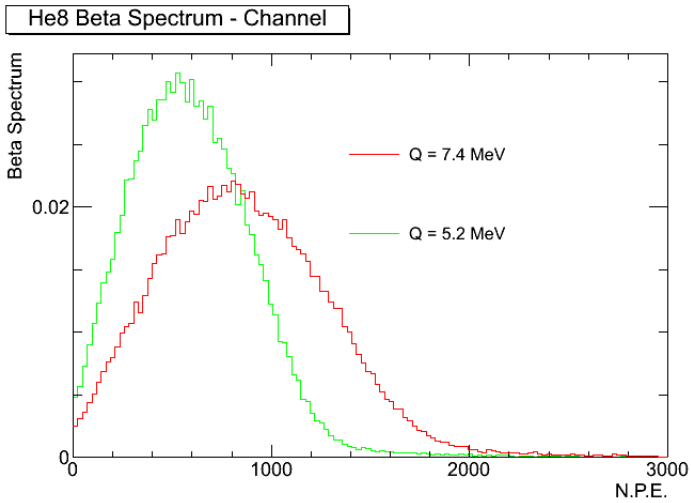

(a) ^{8}He β spectrum for each channel

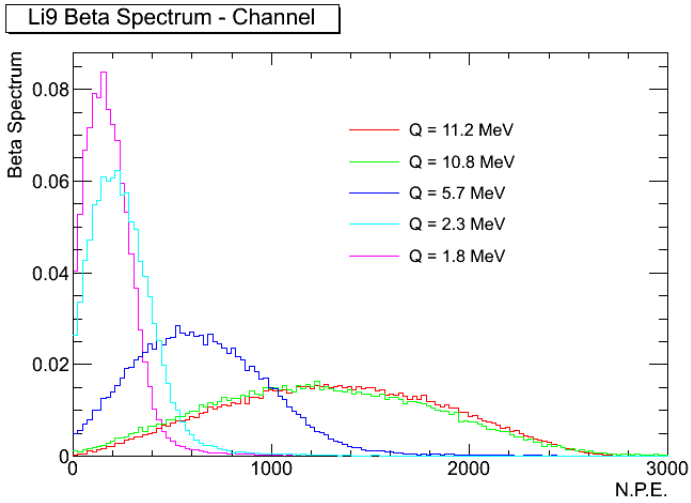

(b) ^{9}Li β spectrum for each channel

Figure 3.6: MC simulation results with n.p.e. distribution. ^{8}He, ^{9}Li only β-n spectrum for each decay channel. 100 thousand events for each decay channel.

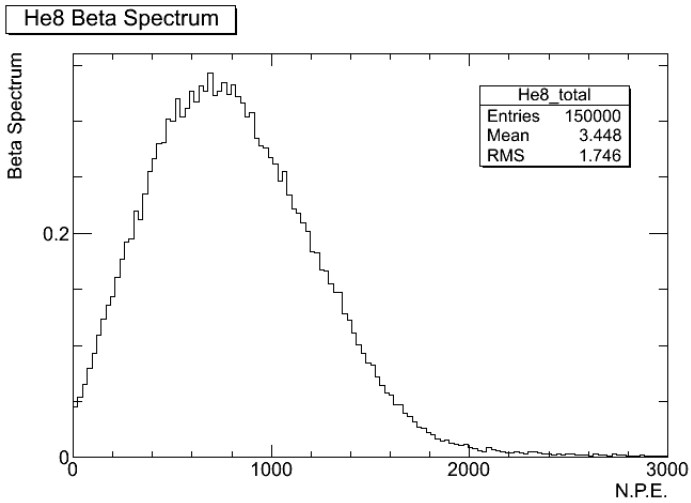

(a) ^{8}He β spectrum for all channels

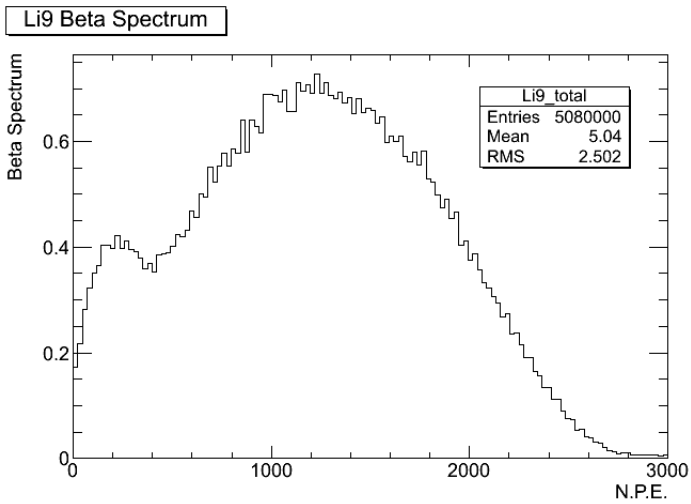

(b) ^{9}Li β spectrum for all channels

Figure 3.7: MC simulation results with n.p.e. distribution. ^{8}He, ^{9}Li only β-n spectrum for total with branching ratio. 100 thousand events for each decay channel.

Chapter 4

Results of MC Simulation on Cosmic Induced ^{9}Li and ^{8}He β-n Decays

4.1 Energy Reconstruction

In this chapter MC simulation results in Chapter 3 are used to fit the ^{9}Li and ^{8}He background data after energy conversion.

Detector gives event signals as number of photoelectrons (NPE) collected by PMTs, instead of energy. So, to converse given NPE to energy is needed to see energy distribution of the event signals. To acquire energy conversion function for MC input simulation, we compare MC input IBD prompt signals with MC output signals. Figure 4.1 shows MC points with error-bar and fit result. Twelve points are fit within $\sim 0.2\%$. Using conversion function, we convert NPE to

energy for all events in our detectors.

The reason that we don't use "p.e. to MeV conversion function" in Chapter 2 is as follows. There are some defects in MC simulation tool. Because the only characteristics of our real detector that we know are copied in MC simulation tool, there may be the other characteristics that we missed. So using just the energy conversion function of real data for MC simulation may cause the misleading results.

The energy converted MC simulation results are shown in Figure 4.2, 4.3. Comparing it with figure 3.4,3.5 of Chapter 3, the difference between random generation and simulation can be checked. Two sets of histograms have same bin size.

4.2 ^{9}Li and ^{8}He Background Data

Background data of ^{9}Li and ^{8}He are obtained considering time correlation with cosmic muon because cosmic muon produces ^{9}Li and ^{8}He. And their characteristic high energy spectrum over 6.5 MeV is also considered.

Impose the muons are randomly distributed in time, the time interval between two adjacent muons follows the relation [22].

$$f_{\mu}(t) = \frac{1}{T}\exp(-\frac{t}{T}) \tag{4.1}$$

where T is the mean time interval between two adjacent muons, $T = 1/\textbf{muon rate}$. The components of muon decay time plot can be divided into mainly two parts, correlated and uncorrelated with cosmic muon. The former is ^{9}Li and ^{8}He background and the latter

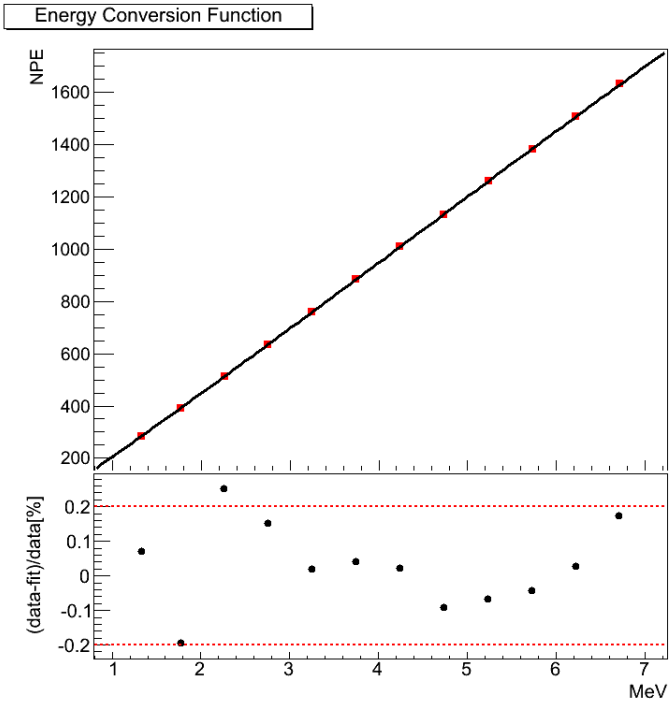

Figure 4.1: Energy conversion function for MC simulation. Twelve points are fit within $\sim 0.2\%$.

are IBD events and other backgrounds uncorrelated with muon. [24]

Fit function is [24]

$$\textbf{Fit function} = B\exp(-\frac{t}{\tau}) + S\exp(-\frac{t}{T}) \tag{4.2}$$

where B,S is fit parameter which means the amplitude of Li/He, IBD/other backgrounds respectively. τ is the life time of ^{9}Li and ^{8}He production. We already know the life time of ^{9}Li and ^{8}He, respectively. So we can get ratio of the production using fit results. But due to the relatively large error, we can only know that ^{9}Li have

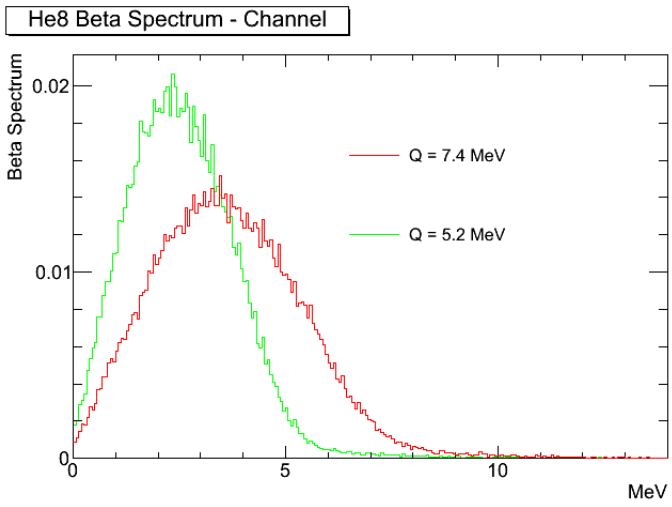

(a) ^{8}He β spectrum for each channel

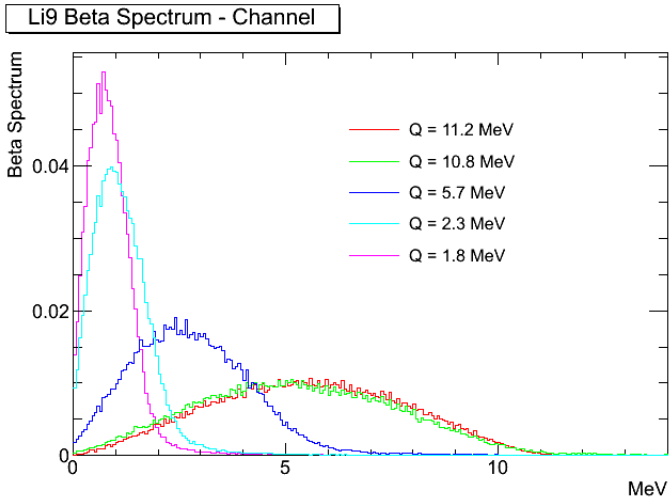

(b) ^{9}Li β spectrum for each channel

Figure 4.2: MC simulation results with energy conversion. ^{8}He, ^{9}Li only β-n spectrum for each decay channel. 100 thousand events for each decay channel.

larger share of the production than ^{8}He. The background data fit results are summarized in Table 4.2.

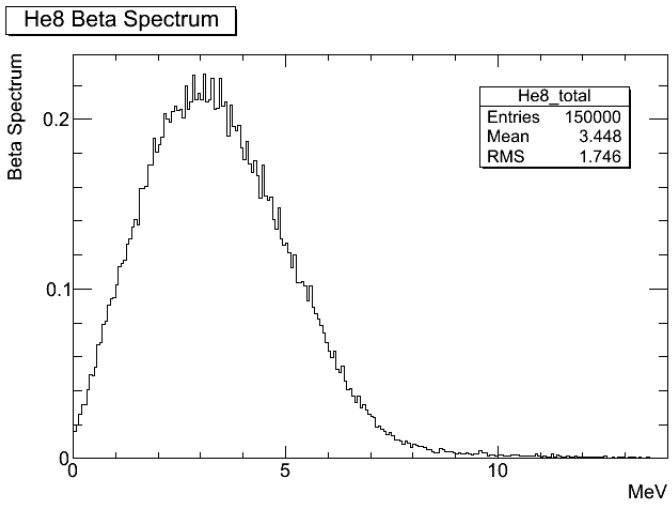

(a) ^{8}He β spectrum for all channels

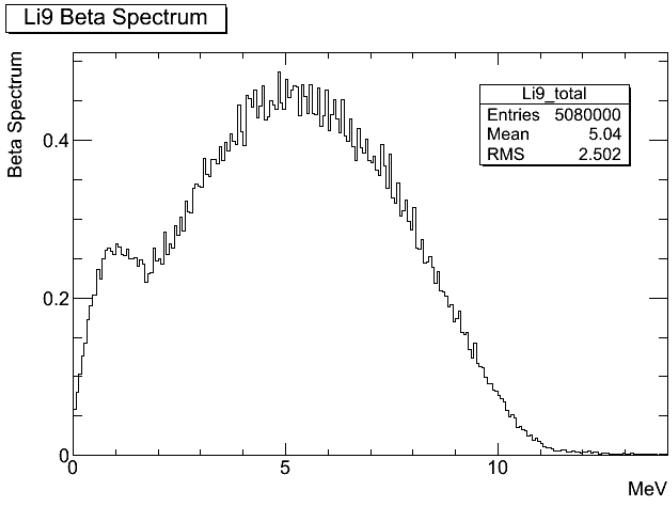

(b) ^{9}Li β spectrum for all channels

Figure 4.3: MC simulation results with energy conversion. ^{8}He, ^{9}Li only β-n spectrum for total with branching ratio. 100 thousand events for each decay channel.

4.3 Comparison with Data

Neutrons are also produced from ^{9}Li and ^{8}He decay. But we fit the

Detector	Far	Near
^{9}Li/^{8}He life time(ms)	212.56±14.19	241.71±25.82

Table 4.1: The ^{9}Li and ^{8}He background data fitting results. This table is taken from [24]

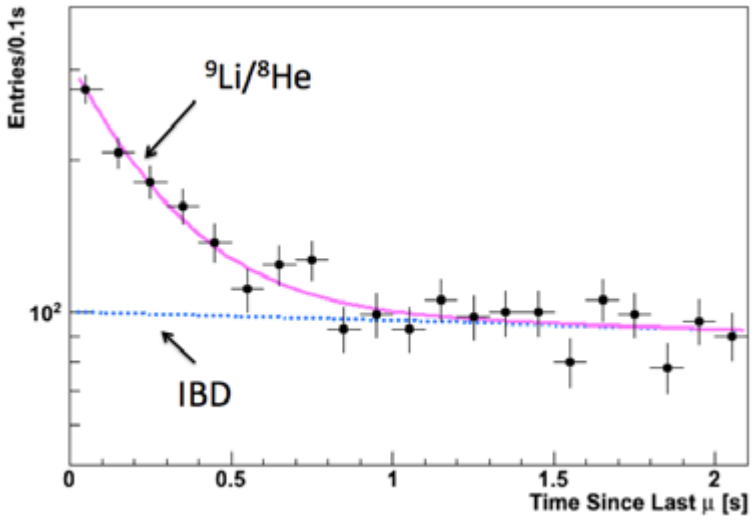

Figure 4.4: ^{9}Li and ^{8}He background data. The data are classified into two parts. One correlated with muon, ^{9}Li and ^{8}He background. The other uncorrelated with muon, IBD events and other backgrounds.

data with only beta spectrum results because neutron gives the definite signals in detector by H or Gd capture after it is thermalized.

To fit ^{9}Li and ^{8}He background data with MC results, we use the method of chi-square minimum. Chi-square fitting is applied as

follows,

$$\chi^2 = \sum_i^n \frac{(x_i - \mu_i)^2}{\sigma_i^2} \tag{4.3}$$

$$\chi^2_{reduced} = \frac{1}{N_{d.o.f}} \sum_i^n \frac{(x_i - \mu_i)^2}{\sigma_i^2} \tag{4.4}$$

where x_i is observed data, μ_i is expected(theoretical) data, σ_i is the error of observed data, and $N_{d.o.f}$ is the number of degrees of freedom, $N_{d.o.f} = N_{points} - N_{fit\ parameter} - 1$.

With data and the error of data fixed, mixing the spectrum of ^{9}Li and ^{8}He by variation of expected data, the minimum of χ^2 is found. And one sigma of chi squared minimum is obtained finding that x values satisfy following condition.

$$\chi^2 - (\chi^2_{min} + 1) = 0 \tag{4.5}$$

where χ means the function value of the chi-square *distribution*. In other words, we translate down chi squared distribution to have -1 minimum value and then find the difference of x values satisfying that distribution equals zero.

Results are shown in Figure 4.5, Figure 4.6. The histograms of these figures have 1 bin per MeV. And because of the energy threshold of prompt signal, data of $0 \sim 1$MeV(first) bin is small particularly so is excluded in fitting.

The minimum values of χ^2 minimum are 4.08153 and 8.6141 %, far, near respectively. The degrees of freedom is (11-1-1)=9, so reduced χ^2 values are 0.4535 and 0.9571 %, far, near respectively. Near site is

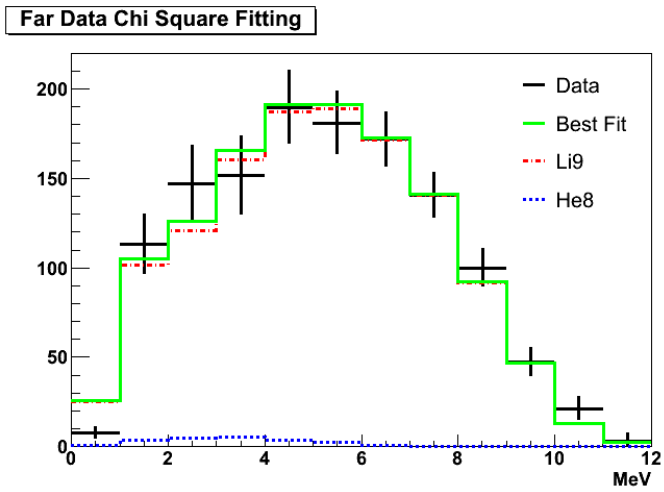

(a) Far site fitting

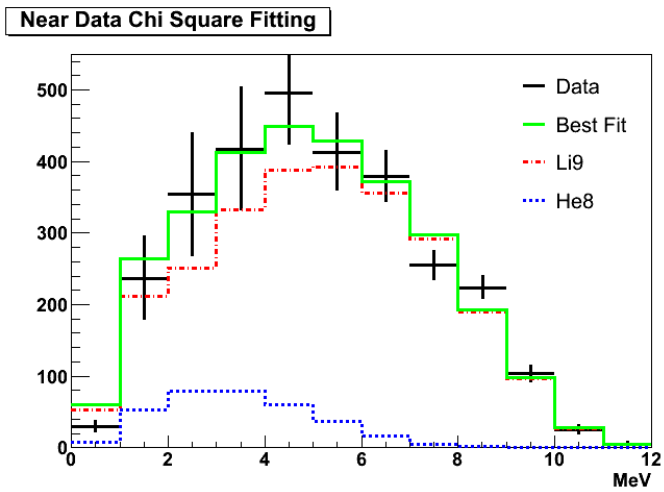

(b) Near site fitting

Figure 4.5: Data fitting with MC result using chi-square method

fitted better than far stie.

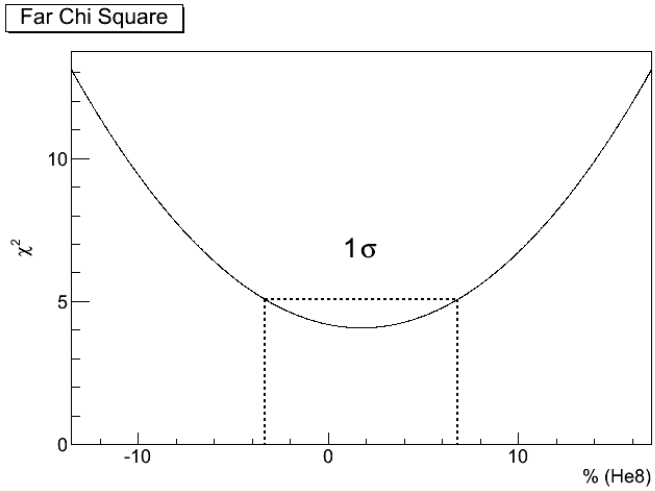

(a) Far site

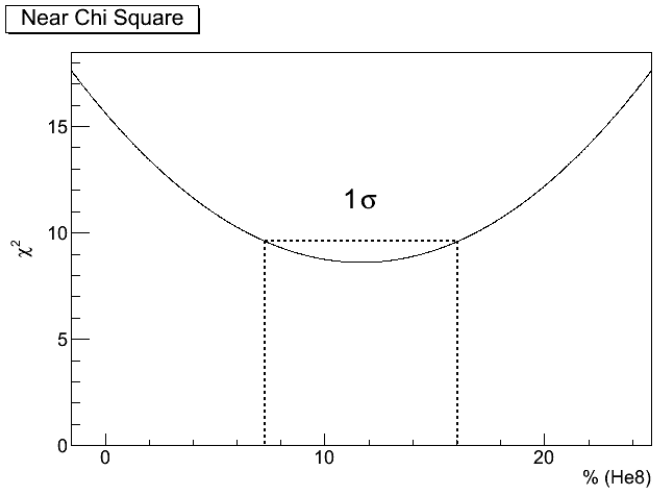

(b) Near site

Figure 4.6: Chi-square distribution

4.4 Measurment of ^{9}Li and ^{8}He Production Ratio

The best fit value of ^{8}He contribution is obtained as 1.73774 $\pm$ 5.07523 (far) or 11.657 $\pm$ 4.39732 (near) %. Therefore, based on this

study, we know that ^{9}Li has much more percentage of ^{9}Li and ^{8}He background in RENO as we expected. The expected half life time of ^{9}Li and ^{8}He background data is 255.321 (far) or 246.877ms (near). The fitting results are summarized in Table 4.2.

Detector	Far	Near
χ^2	4.08	8.61
reduced χ^2	0.454	0.957
life time(ms)	255 $\pm$ 8.74	247 $\pm$ 7.57
^{8}He mixture(%)	1.74 $\pm$ 5.08	11.7 $\pm$ 4.40
^{9}Li mixture(%)	98.3	88.3

Table 4.2: The ^{9}Li and ^{8}He fitting results

The result of near site is similar to that of Table 4.2. But in case of far, in spite of error consideration, difference is big. This discrepancy should be understood.

Because the error of ^{9}Li and ^{8}He background data is decreased as statistics increase, we expect that Chi squared fitting can be better over process of time.

Appendix A

Exponential decay law

If there are disintegrable N particles,

any given particle decay probability per unit time, λ is given by,

$$\lambda = -\frac{1}{N}\frac{dN}{dt} \tag{A.1}$$

It has a clearer meaning when Eq. A.1 is re-expressed by,

$$\lambda N = -\frac{dN}{dt} \tag{A.2}$$

So the number of non-decayed particles at time t is that

$$N(t) = N_0 e^{-\lambda t} \tag{A.3}$$

Probability $p(t)dt$ that decay may occur between t and $t + dt$ is

$$p(t)dt = \frac{|dN(t)/dt|}{\int_0^\infty |dN(t)/dt| dt} dt = \frac{\lambda N_0 e^{-\lambda t}}{N_0} dt = \lambda e^{-\lambda t} dt \tag{A.4}$$

Mean life time τ is given by,

$$\tau = \int_0^\infty tp(t)dt = -te^{-\lambda t} \mid_0^\infty + \int_0^\infty e^{-\lambda t}dt = \frac{1}{\lambda} \tag{A.5}$$

Half life time $\tau_{1/2}$

$$N(t + \tau_{1/2}) = \frac{1}{2}N(t) \tag{A.6}$$

$$\tau_{1/2} = \tau ln2 \tag{A.7}$$

Appendix B

Breit-Wigner formula

In QM, non-relativistic stable state is given by Schrodinger equation,

$$\psi(\vec{r},t) = \psi(\vec{r}) \exp\left[-i\frac{E}{\hbar}t\right]$$

Unstable state is given by, with correction for exponentially decay relation,

$$\psi(\vec{r},t) = \psi(\vec{r}) \exp\left[-i\frac{E}{\hbar}t - \frac{\lambda t}{2}\right]$$

Fourier transform

$$\psi(\vec{r},E) = \psi(\vec{r}) \int_0^\infty \exp\left[i\frac{E-E_0}{\hbar} - \frac{\lambda}{2}t\right] dt$$

$$= \psi(\vec{r}) \frac{1}{\frac{i}{\hbar}(E-E_0) - \frac{\lambda}{2}}$$

$$|\psi(\vec{r},E)|^2 = |\psi(\vec{r})|^2 \frac{1}{\frac{(E-E_0)^2}{\hbar^2} + \frac{\lambda^2}{4}}$$

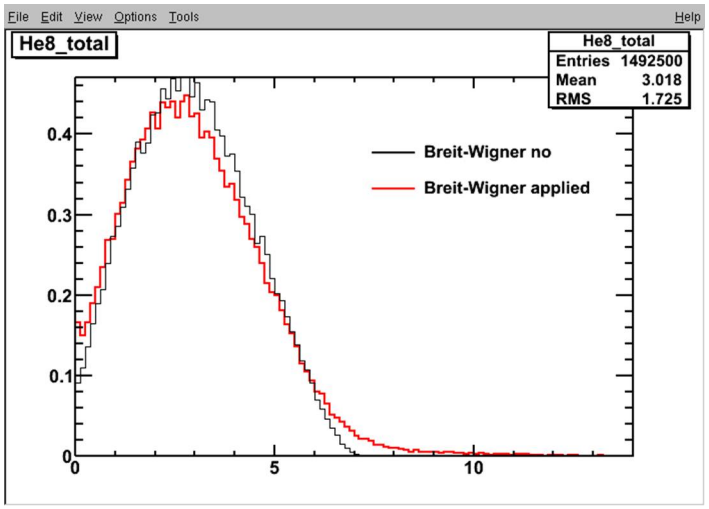

Figure B.1: Before & After Breit-Winger Function applied

$$= |\psi(\vec{r})|^2 \frac{\hbar^2}{(E-E_0)^2 + \frac{\lambda^2\hbar^2}{4}} = |\psi(\vec{r})|^2 \frac{\hbar^2}{(E-E_0)^2 + \frac{1}{4}\left(\frac{\hbar}{\tau}\right)^2}$$

So, probability that a state has energy E,

$$|\psi(E)|^2 \propto \frac{\hbar^2}{(E-E_0)^2 + \frac{\Gamma^2}{4}}$$

$$P(E) = \frac{\Gamma}{2\pi} \frac{\hbar^2}{(E-E_0)^2 + \frac{\Gamma^2}{4}}$$

$$\Gamma \text{ : Decay width, } \Gamma \equiv \frac{\hbar}{\tau}$$

What is mean : By Uncertainty principle,

for stable state $\Delta t = \infty \Rightarrow \Delta E = 0$ the state has definite E

for unstable state $\Delta t = \tau \Rightarrow \Delta E \approx \frac{\hbar}{\tau}$ we can't determine E.

Appendix C

Fermi's Golden rule

β decay's lifetime is far longer than characteristic time, about 10^{-20} s[2]. So β decay causing interaction is far more weak than quasi-stationary interaction, so we can treat it as weak perturbation.

Schrödinger equation for Hamiltonian $H = H_0 + V(t)$ where H_0 is the well known Hamiltonian, $V(t)$ is the weak perturbation,

$$i\hbar\frac{\partial}{\partial t}|\Psi_i(t)\rangle = (H_0 + V(t))|\Psi_i(t)\rangle$$

Another Shrodinger equation for H_0 is,

$$i\hbar\frac{\partial}{\partial t}|\Phi_i(t)\rangle = H_0|\Phi_i(t)\rangle$$

$$V(t)|\Psi_i(t)\rangle \approx V(t)|\Phi_i(t)\rangle$$

$$\left[i\hbar\frac{\partial}{\partial t} - H_0\right]|\Psi_i(t)\rangle = V(t)|\Phi_i(t)\rangle$$

Ansatz

$$|\Psi_i(t)\rangle = |\Phi_i(t)\rangle - \frac{i}{\hbar}\int_{-\infty}^{t} e^{-iH_0(t-t')/\hbar}V(t')|\Phi_i(t')\rangle dt'$$

$$A_{i\to f} = \langle\Phi_f(t)|\Phi_i(t)\rangle - \frac{i}{\hbar}\int_{-\infty}^{t}\langle\Phi_f(t)|e^{-iH_0(t-t')/\hbar}V(t)|\Phi_i(t')\rangle dt'$$

in time independent perturbation case, $V(t) = V$, such as a particle scattering,

$$A_{i\to f} = -\frac{i}{\hbar}\int_{-T}^{T}\langle\Phi_f(t)|e^{-iH_0(t-t')/\hbar}V|\Phi_i(t')\rangle dt'$$

$$i\hbar\frac{\partial}{\partial t}|\Phi_{i,f}(t)\rangle = E_{i,f}|\Phi_{i,f}(t)\rangle$$

$$A_{i\to f} = -\frac{i}{\hbar}\langle\Phi_f|V|\Phi_i\rangle\int_{-T}^{T} e^{-i(E_f-E_i)t'/\hbar}dt'$$

$$P_{i\to f} = \frac{4}{\hbar^2}\left|\langle\Phi_f|V|\Phi_i\rangle\right|^2\frac{\sin^2(\omega_{fi}T)}{\omega_{fi}^2}$$

$$\int_{-\infty}^{\infty}\frac{\sin^2(\omega_{fi}T)}{\omega_{fi}^2}d\omega_{fi} = \pi T$$

When $T \to \infty$

$$\frac{\sin^2(\omega_{fi}T)}{\omega_{fi}^2} d\omega_{fi} = \pi T \delta(\omega_{fi})$$

$$P_{i\to f} = \frac{2\pi}{\hbar^2} \left|\langle \Phi_f | V | \Phi_i \rangle\right|^2 \delta(E_f - E_i)(2T)$$

$$\dot{P}_{i\to f} = \frac{2\pi}{\hbar^2} \left|\langle \Phi_f | V | \Phi_i \rangle\right|^2 \delta(E_f - E_i)$$

When final state has continuous energy eigenstates,

$$\dot{P}_{i\to F} = \frac{2\pi}{\hbar^2} \left|\langle \Phi_f | V | \Phi_i \rangle\right|^2 \rho(E_f)$$

So, the transition rate λ is

$$\lambda = \frac{2\pi}{\hbar^2} \left|\langle \Phi_f | V | \Phi_i \rangle\right|^2 \rho(E_f)$$

This chapter C follows content development of [25].

Appendix D

KPS Poster

Stability of energy calibration at RENO

이 순규 (발표자 학생), 김 수봉, 김 상용, 박 정식, 서 선희, 서 현관, 이 동하, 최 선호, 최 원국, 김 우영[1], 세르게이 체바토료프[1], 박 인곤[2], 장 지승[3], 박 명렬[4], 최 준호[4], 안 정근[5], 박 강순[6], 장 한일[7], 양 장희[8], 유 인태[8], 최 영일[8], 김 영덕[9], 마 경주[9], 전 은주[9], 김 바로[10], 박 령균[10], 김 재률[10], 소 선행[10], 송 숙형[10], 신 창동[10], 여 인성[10], 임 인택[10], 주 경광[10], 김 현수[11], 김 시연[12], 고 영주[12]

서울대학교. [1]경북대학교. [2]경상대학교. [3]광주과기원. [4]동신대학교. [5]부산대학교. [6]서경대학교. [7]서영대학교. [8]성균관대학교. [9]세종대학교. [10]전남대학교. [11]전북대학교. [12]중앙대학교

Calibration System and Radioactive Sources

» Calibration

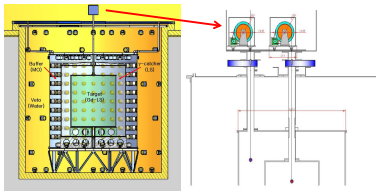

To Calibrate Detector response for the Inverse Beta Decay, we use the radioactive sources.

» Detector Response

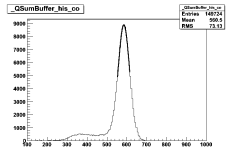

Radioactive source (Ex. ^{60}Co)

» Radioactivity source

Source	Type	Energy (KeV)	Calibration
^{68}Ge	e^+	511(2)	Positron
^{137}Cs	γ	662	Gamma
^{60}Co	γ	1173 + 1333	Multiple Gamma
^{252}Cf	n	Neutron + ~10MeV	Neutron efficiency

Time Variation of Measured Charges from Sources

» Total charge of buffer

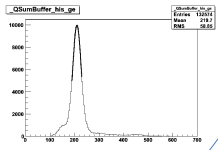

Peak value of total charge distribution

There are two rapid decreases because of Flasher PMT(s) removal.

FAR

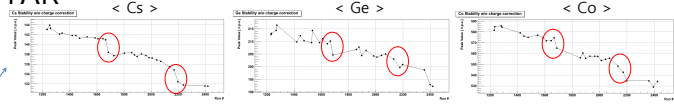

NEAR

Period : 2012 07 ~ 2013 10

○ : Disconnect Flasher(abnormal) PMT(s)

Stability of Energy Calibration

Modified with charge correction.

Distribution of data is almost flat considering fluctuation.

After calibration and applying charge correction, our data are stable.

FAR

NEAR

Period : 2012 07 ~ 2013 09

FAR

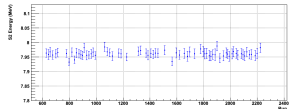

NEAR

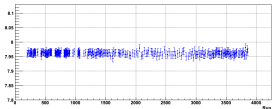

Period : 2011 09 ~ 2013 09

Study of cosmic-ray induced Li & He production at RENO

Sunkyu Lee on Behalf of RENO Collaboration
Seoul National University

INTRODUCTION

When cosmic moun strikes ^{12}C in liquid scintillator passing through detector, unstable isotopes are produced such as $^{9}Li/^{8}He$. This cosmogenic isotopes $^{9}Li/^{8}He$ are backgrounds in the RENO experiment for detecting reactor antineutrino. **Background** is the signal mimicking inverse beta decay(IBD)'s.
IBD - The produced positron immediately annihilates and emits two gammas with visible energy called prompt signal. And the neutron is thermalized and then captured by Gd emitting additional gammas. This process takes average time about 30μs , called delayed signal.
^{9}Li and ^{8}He has several β-neutron emission decay modes which gives signal mimicking prompt and delayed signal respectively.
So this kind of background is indistinguishable from IBD signal unless using additional condition

IBD Signal

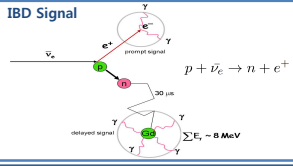

$^{9}Li/^{8}He$ Background

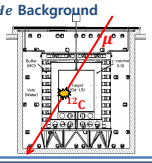

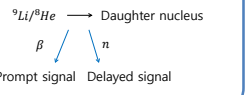

CHARACTERISTICS OF $^{9}Li/^{8}He$ β-n DECAY

Characteristics of $^{9}Li/^{8}He$

^{9}Li and ^{8}He have mean lifetime 257ms and 172ms, respectively.
The Q values of 9Li and 8He decay are 13.61MeV and 10.65MeV overlapping with prompt(positron) signal of IBD.
Some emitters of 9Li and 8He have sufficient energy for neutron decay which can be captured by Gd. And this neutron decay occurs immediately because it competes with γ decay.

Decay Channel of $^{9}Li/^{8}He$

Parent	Daughter or Emitter	Width(MeV)	Branching ratio	β	neutron
^{9}Li	^{9}Be (ground)	0	48.7	○	
^{9}Li	^{9}Be (2.43MeV)	0.00077	30	○	○
^{9}Li	^{9}Be (2.78MeV)	1.08	16	○	○
^{9}Li	^{9}Be (7.94MeV)	1.0	1.5	○	○
^{9}Li	^{9}Be (11.28MeV)	0.575	1.1	○	○
^{9}Li	^{9}Be (11.81MeV)	0.400	2.7	○	○
^{8}He	^{8}Li (0.98MeV)	0	84	○	
^{8}He	^{8}Li (3.21MeV)	1.0	12	○	○
^{8}He	^{8}Li (5.4MeV)	0.65	4	○	○

β-n decay mode

Beta Spectrum Shape

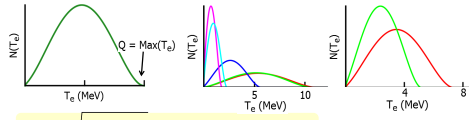

$$N(T_e) \propto \sqrt{T_e^2 + 2m_e T_e (T_e + m_e)(Q - T_e)^2 F(Z_d, T_e)}$$

T_e : Kinetic energy of electron
m_e : Mass of electron
Z_d : Atomic number of daughter nucleus
$F(Z_d, T_e)$: Fermi Function

MC SIMULATION

Energy Conversion

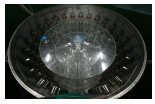

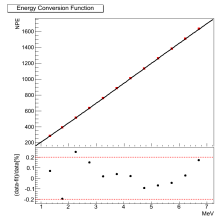

Detector gives event signals as number of photoelectrons (NPE) collected by PMTs, instead of energy.
So, to converse given NPE to energy is needed to see energy distribution of the event signals.
To acquire energy conversion function for MC input simulation, we compare MC IBD prompt(positron) signals with output signals. MC points with error-bar and fit result. Twelve points are fit within 0.2%

Detector Simulation

^{9}Li Beta Spectrum

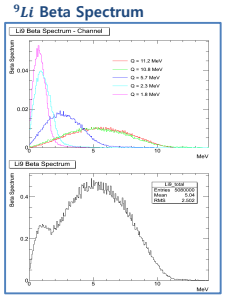

^{8}He Beta Spectrum

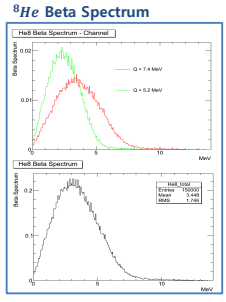

Beta spectrums each decay channel and total spectrum with branching ratio. After detector simulation, resolution of detectors and attenuation in liquid scintillator etc. detector characteristics are applied.

DATA COMPARISON

Far Detector

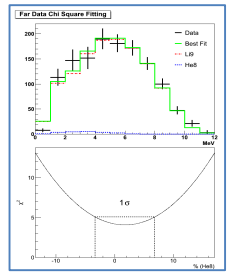

Near Detector

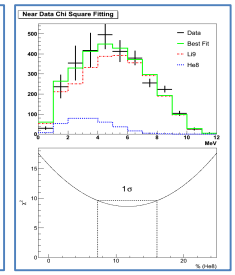

Data set and MC results are fitted using χ^2 fitting.
χ^2 minimum value is 4.08153, 8.6141% far, near site respectively.
So, χ^2 fitting is better in near site than far site.

Estimated ratio of $^{9}Li/^{8}He$ production
Far : 98.26(%,^{9}Li) + 1.738(%,^{8}He)
Near : 88.34(%,^{9}Li) + 11.66(%,^{8}He)
Therefore, ^{9}Li is the most component of $^{9}Li/^{8}He$ background data in RENO.
The expected half life time of $^{9}Li/^{8}He$ background data is 255.3, 246.8ms, far and near respectively.

Bibliography

[1] K. Anderson, J. Anjos, D. Ayres, J. Beacom, I. Bediaga, *et al.*, "White paper report on Using Nuclear Reactors to Search for a value of θ_{13}," 2004.

[2] S.-B. Kim, T. Lasserre, and Y. Wang, "Reactor neutrinos," *Adv.High Energy Phys.*, vol. 2013, p. 453816, 2013.

[3] J. Ahn *et al.*, "RENO: An Experiment for Neutrino Oscillation Parameter θ_{13} Using Reactor Neutrinos at Yonggwang," 2010.

[4] J. Ahn *et al.*, "Observation of Reactor Electron Antineutrino Disappearance in the RENO Experiment," *Phys.Rev.Lett.*, vol. 108, p. 191802, 2012.

[5] B. Pontecorvo, "Inverse beta processes and nonconservation of lepton charge," *Sov.Phys.JETP*, vol. 7, pp. 172–173, 1958.

[6] B. Pontecorvo, "Mesonium and anti-mesonium," *Sov.Phys.JETP*, vol. 6, p. 429, 1957.

[7] Z. Maki, M. Nakagawa, and S. Sakata, "Remarks on the unified model of elementary particles," *Prog.Theor.Phys.*, vol. 28, pp. 870–880, 1962.

[8] H. Minakata and S. Watanabe, "Solar neutrinos and leptonic CP violation," *Phys.Lett.*, vol. B468, pp. 256–260, 1999.

[9] H. Minakata, H. Sugiyama, O. Yasuda, K. Inoue, and F. Suekane, "Reactor measurement of theta(13) and its complementarity to long baseline experiments," *Phys.Rev.*, vol. D68, p. 033017, 2003.

[10] K. Awai, Y. Hayato, K. Kaneyuki, S. Nakayama, H. Nishino, *et al.*, "Development of New Front-End Electronics for Super-Kamiokande," *Nuclear Science Symposium Conference Record, 2007. NSS '07. IEEE*, vol. 1, pp. 127–132, 2007.

[11] H. Nishino, K. Awai, Y. Hayato, S. Nakayama, K. Okumura, *et al.*, "High-speed charge-to-time converter ASIC for the Super-Kamiokande detector," *Nucl.Instrum.Meth.*, vol. A610, pp. 710–717, 2009.

[12] K. Park, "1d & 3d calibration system," *15th RENO Collaboration meeting*, 2011.

[13] S.-H. Seo, "New Results from RENO," 2013.

[14] F. Ajzenberg-Selove, "Energy levels of light nuclei A = 5-10," *Nucl.Phys.*, vol. A490, pp. 1–225, 1988.

[15] G. Nyman *et al.*, "The Beta Decay of ^{9}Li to Levels in ^{9}Be: A New Look," *Nucl.Phys.*, vol. A510, p. 189, 1990.

[16] F. Barker and E. Warburton, "The beta-decay of ^{8}He ," *Nuclear Physics A*, vol. 487, no. 2, pp. 269 – 278, 1988.

[17] T. Björnstad, H. Gustafsson, B. Jonson, P. Larsson, V. Lindfors, S. Mattsson, G. Nyman, A. Poskanzer, H. Ravn, and D. Schardt, "The decay of ^{8}He ," *Nuclear Physics A*, vol. 366, no. 3, pp. 461 – 468, 1981.

[18] M. Borge *et al.*, "BETA DELAYED TRITON EMISSION IN THE DECAY OF He-8," *Nucl.Phys.*, vol. A460, pp. 373–380, 1986.

[19] K. Krane, *INTRODUCTORY NUCLEAR PHYSICS*. 1987.

[20] E. Fermi, "An attempt of a theory of beta radiation. 1.," *Z.Phys.*, vol. 88, pp. 161–177, 1934.

[21] F. L. Wilson, "Fermi's theory of beta decay," *American Journal of Physics*, vol. 36, no. 12, pp. 1150–1160, 1968.

[22] L.-j. Wen, J. Cao, K.-B. Luk, Y.-q. Ma, Y.-f. Wang, *et al.*, "Measuring cosmogenic Li-9 background in a reactor neutrino experiment," *Nucl.Instrum.Meth.*, vol. A564, pp. 471–474, 2006.

[23] W. Leo, *Techniques for Nuclear and Particle Physics Experiments: A How to Approach*. 1987.

[24] W. Choi, "Li/he background for 800days of reno data," *RENO Internal note*, 2014.

[25] K. Gottfried, *Quantum Mechanics: Fundamentals*. Springer New York, 2003.

국문 초록

RENO 실험은 중성미자 진동상수 θ_{13}를 구하기 위해 원자로를 이용하는 실험이다. θ_{13}를 성공적으로 측정하기 위해서는 몇가지가 필요하다. 그 중 한가지가 실험기간 동안, 정기적인 검출기의 에너지 보정이다. 검출기 에너지 보정을 통해서 RENO 실험 시작일인 2011년 8월부터 2014년 4월까지 오차범위 약 1.3% 이내 일정한 검출기 반응을 얻었다.

성공적인 실험을 위한 다른 한가지는 반중성미자 검출의 Background를 줄이는 것이다. 우주선(cosmic-ray)으로 생긴 리튬과 헬륨의 베타-중성자 붕괴는 RENO의 가장 큰 Background이다. 몬테 카를로 시뮬레이션을 통해 리튬 헬륨 Background를 연구하였고 검출기의 리튬, 헬륨 비율을 예측하였다. 비율은 리튬 헬륨 각각 원거리 검출기의 경우 98.3%, $1.74 \pm 5.08\%$, 근거리 검출기의 경우 88.3%, $11.7 \pm 4.40\%$를 얻었다.

주요어 : **RENO, 중성미자 진동, θ_{13}, 에너지 보정, 몬테 카를로 시뮬레이션, 리튬 헬륨 Background**

학 번 : 2011-23277